I give permission for public access to my thesis for any copying to be done at the

discretion of the archives librarian and/or the College librarian.

Signature:_____ Date: _____

1. ABSTRACT

Photo-crosslinkable hydrogel films are versatile materials for controlled drug delivery devices (Duncan, 2003), three-dimensional micro-assemblies, and components in microfluidic systems (Beebe *et al.*, 2000). A hydrogel is a flexible network of polymer molecules which swells when placed in water but will not dissolve because of the chemical or physical interconnections, called crosslinks, between the long chains of polymer molecules. Because of the high water content, hydrogels are pliable and respond to environmental conditions since the degree of swelling in these networks depends on environmental conditions such as pH and temperature (Hilt *et al.*, 2003). This flexibility and environmental sensitivity renders hydrogels versatile materials for applications. For instance, the probability that they will damage delicate system components during micro-assembly is lower, and they can be tailored to respond to specific environments. Consequently, it is important to understand both the mechanical properties and the dynamics responses of these materials when designing such applications. Therefore, my thesis uses an atomic force microscope (AFM) to measure indentation with each applied force and then determines the best model with which to determine the mechanical properties from these data.

Hydrogels also have poroelastic and viscoelastic properties which affect stress relaxation and thus impact their behavior in the different applications above. On short time scales, viscoelastic materials respond to stresses as elastic solids. On longer time scales, however, viscoelastic materials behave under stress

as viscous fluids (Lin, 51). In poroelastic materials, the fluid in the material migrates simultaneously with the deformation of the porous network (Cai *et al.*, 2010). Relatively recently, poroelasticity has been identified as an important factor in the mechanical behavior of polymer gels (Galli *et al.*, 2008).

Photo-crosslinkable hydrogels are unique because they crosslink – the polymer chains bond to form the network – when exposed to ultraviolet (UV) light. Different dosages of UV light produce different mechanical properties, a feature which can be utilized when designing systems (Toomey *et al.,* 2004). Although the mechanical properties of hydrogels have been studied extensively, the mechanical properties of photo-crosslinkable hydrogels have not been investigated thoroughly. To design accurate controlled drug delivery devices and other applications, we must both understand the stress relaxation of photo-patterned hydrogels and correlate the UV dosage and mechanical properties.

We use AFM to examine the mechanical properties of poly(*N*-isopropylacrylamide) (PNIPAm), which is attached to a silanized silicon substrate with a HEMA adhesive layer. We primarily use the AFM to collect force versus indentation data. In order to extract mechanical properties, particularly the Young's modulus (the ratio of stress to strain) of the materials, from these data, we will evaluate existing mechanical models. Originally, the Hertz model (Hertz, 1881) was used to correlate the indentation and force data to the mechanical properties of the materials. This model, however, does not consider the surface forces between the two contacting surfaces, rendering it inaccurate for hydrogel

thin films, where surface forces are significant. The Johnson, Kendall, and

Roberts model (Johnson *et al.*, 1971), which includes surface forces, is more

appropriate but does not account for viscoelastic and poroelastic effects.

Therefore, we will evaluate these models and modify them as needed to account

for the poroelasticity of hydrogels. Simultaneously, we study the stress relaxation

in these materials in the context of the viscoelastic and poroelastic relaxation

models.

Mechanical Characterization

of Photo-crosslinkable Hydrogels

with AFM

Alyssa McKenna

Katherine Aidala, Mount Holyoke College
Thesis Advisor

Ryan Hayward, University of Massachusetts Amherst
Thesis Advisor

2. ACKNOWLEDGEMENTS

First, I have to thank my two advisers, Kathy Aidala and Ryan Hayward. Because of Kathy's encouragement, insight, and occasional large dose of perspective, I have realized that I love Physics and want to pursue science in my career with her dedication. Watching her zeal for science and for helping her students, I learned that a truly great professor always expects more of each student than she ever thought possible and never lets a student's question go unanswered. Because of Ryan's willingness to take me on in his research lab for a summer, I learned the importance of perseverance and patience in research and discovered materials science, a field which satisfied two of my fascinations: *why* materials act the way they do and *what* cool new applications we can make with them! In all of our discussions about polymers and the associated "challenges," I quickly realized that the hallmark of a great scientist is the creativity to use unusual means and materials to solve practical problems.

I want to thank Mark Peterson for being an enthusiastic member of my committee. Without his support, this thesis would not have been possible.

I have to thank Dr. MyungHwan Byun at the University of Massachusetts Amherst for fabricating my samples. In addition, I am so grateful to Professor Anne Murdaugh, now a professor at Rollins College, who taught me how to use the AFM and frequently helped me troubleshoot when she was a postdoc in Kathy Aidala's lab.

I am so grateful to the Physics department for providing me the

opportunity to study physics. I have to thank all the professors, but especially Janice Hudgings, Neal Abraham, and Mark Peterson, for their passion for teaching and for Physics. Also, thank you to Cindy Morrell and Sarah Byrne, for keeping the whole department welcoming and organized.

I am so blessed to have all my friends at Mount Holyoke who have seen me laugh, rant, and cry but still *want* to eat dinner with me. In particular, I have to thank Meeraal for teaching me to meet all life's adventures with an open heart and laughter, Katie for inspiring me with her quiet passion for helping others no matter how tired she herself is, San for showing me that all aspects of life are wonderful, and Emma for being the loyal, passionate, and dramatic woman I hope my future daughters will be. A special acknowledgement must also be given to all the wonderful Physics majors – San, Amy, Emily, Sarah, Gloria, Xiaolin, Hexuan, Kim, Phoebe, Alena, Qinxia, Ruimin, Sophia – who have stayed up with me until 3 a.m. in the Physics lounge and made me laugh about that homework set rather than cry like I wanted to.

Finally, I have to thank my family – Mommy, Daddy, Brent, and Sunny. Thank you for being the support system I need when I am otherwise too scared to pursue my dreams but giving me the freedom to explore. Thank you for inspiring me, scolding me, teasing me, and loving me, no matter what. I cannot live without you all.

TABLE OF CONTENTS

LIST OF FIGURES AND TABLES

3. INTRODUCTION

OVERVIEW

This chapter will outline the fundamentals of polymer science, mechanics, and

hydrogels which pertain to this research. I will first introduce the foundational

terms describing polymers and second introduce hydrogels. In section 3.1.2

discussing hydrogels, I will describe the process of photo-crosslinking, which

motivates this research. I will then summarize important vocabulary from studies

of mechanics and of materials mechanics. Next, I will highlight several

applications of hydrogels, particularly the use of hydrogels as components of

microfluidic systems and as controlled drug delivery devices. Finally, I will

outline the motivation and objectives of this thesis work and summarize the

research accomplished.

3.1. HYDROGELS AND THEIR MATERIAL PROPERTIES

3.1.1 BASIC DEFINITIONS REGARDING POLYMERS

A polymer is a long molecule constructed of monomers, where a monomer

is any one unit of the repeating chemicals bonded together to form the polymer

molecule (Lin, 1). In the polymer molecule itself, the structural unit which each

monomer forms and which is eventually bonded with other units to form the

polymer is called the monomeric segment, and its chemical structure is known as

the microstructure (Lin, 1). A polymer can be either a homopolymer – in which

all the monomers in the polymer are identical (Cowie *et al.*, 3) – or a copolymer –

in which the polymer is made up of two or more different monomers (Lin, 1).

The polymer that I investigated in this research is poly(*N*-isopropyl

acrylamide-co-acrylamidobenzophenone-co-acrylic acid-co-tetramethyl

rhodamine isothyocyanate), abbreviated henceforth PNIPAm, a copolymer with

four different monomeric segments as shown below in Figure 3.1.1. In PNIPAm,

the four monomers are *N* -isopropylacrylamide, acrylamidobenzophenone, acrylic

acid, and Rhodamine B methacrylate. The acrylamidobenzophenone enables the
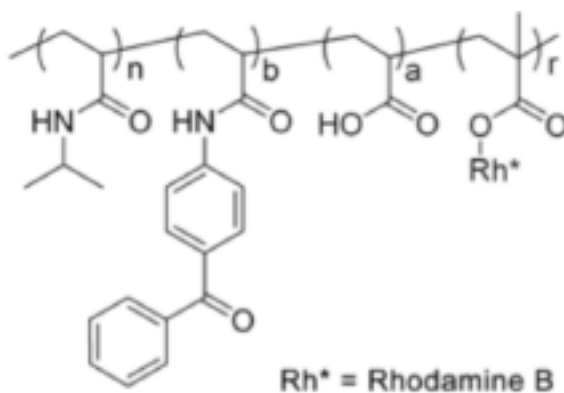
Figure 3.1. 1: Chemical structure of PNIPAm
copolymer used in this study

hydrogel to be crosslinked using benzophenone photo-chemistry (photo-

crosslinking), which is described in section 3.1.2. The acrylic acid lends the

hydrogel charge, which allows the hydrogel to swell more. Finally, Rhodamine B

is the fluorescent dye that allows the hydrogel to be optically imaged in other

research in the Hayward group at the University of Massachusetts Amherst.

Polymers exhibit viscoelastic behavior when stress is applied. As the

name suggests, viscoelastic materials exhibit both viscous and elastic behavior. On long time scales, the polymer behaves as a viscous fluid. In other words, when a stress is applied over a long time interval either increasing gradually or held constant, the polymer chains flow away from the point where the stress is being applied (Cowie *et al.*, 345-346). This deformation is irreversible because the polymer chains must disentangle in order to flow. Consequently, the rate of flow depends on this rate of disentanglement and the rate at which the polymer chains are able to slide past one another (Carraher, 374).

In contrast, on short times scales, the polymer behaves as an elastic solid. In particular, when stress is applied quickly, the covalent bonds holding the polymer together elongate reversibly. The bond angles are distorted, but the polymer network is not pulled apart, resulting in a net, reversible elongation of the polymer sample. Even later as the polymer chains begin to straighten out as a result of prolonged strain, this elongation remains reversible (Carraher, 374). Because the polymer chains do not have time to disentangle fully to flow, the material will behave elastically, meaning that it will return to its initial configuration when the applied stress is removed (Cowie *et al.*, 345-346). Obviously, the response of viscoelastic polymers to stress will be time-dependent (Cowie *et al.*, 349-357).

3.1.2. HYDROGEL

A gel or hydrogel is a network of polymer molecules connected by

chemical or physical interconnections, called crosslinks, with a high solvent content (Hilt *et al.*, 2003). For PNIPAm, the crosslinks are covalent bonds. The process of inducing the individual polymer chains to form these covalent bonds with adjacent chains is called crosslinking (Carraher, 43). As shown in Figure 2, when exposed to 365 nm ultraviolet (UV) light, the pendant benzophenone units incorporated onto the polymer chain in the copolymer PNIPAm in this study are activated, and the polymer crosslinks, forming a hydrogel. Due to this characteristic, the PNIPAm films in this research are called photo-crosslinkable hydrogels.

Photo-crosslinking offers a safer, versatile technique compared to conventional crosslinking techniques. First, photo-crosslinking requires only a UV light source rather than the chemicals (Carraher, 43) or heat (i.e., vulcanization (Cowie *et al.*, 391)) used in conventional crosslinking. Therefore, photo-crosslinking offers a safer alternative to current patterning techniques, which can require harsh chemicals (Hilt *et al.*, 2003). More importantly, photo-crosslinking allows scientists to pattern microscale features onto the hydrogel film and to control the crosslinking density of those features. This characteristic offers scientists the opportunity to design microfluidic components and potentially microassembly devices easily and efficiently (Kim *et al.*, 2010).
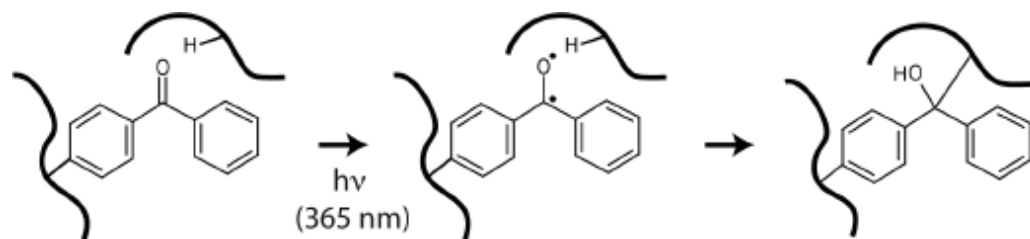
Figure 3.1. 2: In photo-crosslinking, the 365 nm light induces covalent bonds to form between adjacent polymer molecules, thereby crosslinking the film.

Crosslinks lend the hydrogel structure and give it "memory" as well as unique physical properties (Carraher, 43). Although the hydrogel has a high fluid content, the crosslinks allow the hydrogel to retain its shape when not under stress and to return to its shape when stress is released (Carraher, 43-46). As the crosslink density – the number of crosslinks in a unit volume of the network – increases, the hydrogel has more connections holding it in a particular shape, making it less and less pliable (Cowie *et al.*, 391).

Because of the high solvent content, hydrogels are pliable and respond to environmental conditions since environmental stimuli, such as pH and temperature, control the amount of solvent that hydrogel absorbs (Hilt *et al.*, 2003; Kim *et al.*, 2010). PNIPAm is known to be particularly responsive to temperature changes. More specifically, PNIPAm hydrogels deswell as the temperature is increased (Kim *et al.*, 2010).

In addition to viscoelastic behavior, hydrogels exhibit poroelastic behavior. In poroelastic materials, the solvent in the material migrates simultaneously with the deformation of the porous network (Cai *et al.*, 2010). Thus, we expect a time-dependence in the response of the gel to a deforming force (Cai *et al.*, 2010). When a poroelastic material is compressed suddenly, the solvent in the gel initially does not have time to migrate, and the force on the indenter immediately and dramatically increases.   But if the resulting indentation into the gel is subsequently maintained, the solvent begins to migrate away from

the indentation, and the force on the indenter decreases accordingly. The force on

the indenter approaches a constant value asymptotically as the solvent in the gel

reaches a new equilibrium (Cai, *et al.*, 2010, 1). Relatively recently,

poroelasticity has been identified as an important factor in the mechanical

behavior of polymer gels (Galli *et al.*, 2008).

3.1.3 MECHANICAL PROPERTIES AND TERMS

The study of mechanical properties of materials can be traced back to the

experiments of Galileo in the early seventeenth century. By the following

century, mechanical characterization techniques and vocabulary had begun to be

developed. Consequently, we must understand the vocabulary of mechanical

properties (Hibbeler, 4) as well as the molecular behavior of polymers in order to

describe the mechanical properties of PNIPAm accurately.

Stress is the applied force per unit area. The term "stress" includes **normal**

stress, the applied force acting normal to an area of interest per unit area

and represented with σ (Hibbeler, 23), and **shear stress**, the applied force

acting tangental to an area of interest per unit area and represented with τ

(Hibbeler, 23). Stress has units of pascals (Pa) or Newtons per square

meter (N/m^2) (Hibbeler, 23).

Load is the applied force (Hibbeler, 4).

Strain is the ratio of the deformation of an object in one dimension (such as

length) and the original size of the object in that same dimension. Like

stress, "strain" includes **normal strain**, the change in length of an object

divided by the original length and represented by ε (Hibbeler, 68), and

shear strain, the change in angle between two segments of the object

initially normal to one another and represented by γ (Hibbeler, 69).

Normal strain is dimensionless but may be expressed as a ratio of units

(e.g., m/m) or as a percentage (e.g., 0.1 m/m = 10%) (Hibbeler, 69). Shear

strain is measured in radians (Hibbeler, 69).

Young's modulus or modulus of elasticity is the constant of proportionality

relating normal stress and normal strain when normal stress

and strain are linearly proportional. Although polymers are

viscoelastic, the normal stress and strain can be approximated

as linear on short time scales when the strains are small and the

deformation is therefore reversible (Kranenburg *et al.*, 2009).

for uniaxial deformation under these conditions, Hooke's law

describes the relationship between stress, strain, and the

Young's modulus:

$$\sigma = E\varepsilon \qquad\qquad (3.1)$$

where E is Young's modulus and has the units of normal stress,

pascals (Hibbeler, 92).

Shear modulus or shear modulus of elasticity or modulus of rigidity is the

constant of proportionality relating shear stress and shear strain

when shear stress and strain are linearly proportional. In

materials which obey Hooke's law:

$$\tau = G\gamma \qquad (3.2)$$

where G is the shear modulus (Hibbeler, 106).

Poisson's ratio is the negative of the ratio of longitudinal strain to lateral strain.

In the case of an axial tensile (pulling) force, the object will

elongate in the longitudinal direction (positive strain) and contract

in the lateral direction (negative strain). Poisson's ratio is the

ratio of these two strains (Hibbler, 104). Because of the minus

sign, Poisson's ratio, however, is always positive. In addition,

Poisson's ratio is dimensionless. During elastic deformation,

Poisson's ratio is a constant (Hibbeler, 86, 104). When the

material is both homogeneous and isotropic, Poisson's ratio is

related to the longitudinal and lateral strains by:

$$v = -\frac{\varepsilon_{lat}}{\varepsilon_{long}} \qquad (3.3)$$

Poisson's ratio has a value of 0 for an ideal material which does

not move laterally when it is subjected to tensile or compressive

stress. Its maximum value is 0.5 (Hibbeler, 104). For rigid,

elastic solids, in which the volume does not change during

deformation, Poisson's ratio v has a value of 0.5 (Carraher, 374).

The Young's modulus, shear modulus, and Poisson's ratio are

related by

$$G = \frac{E}{2(1 + v)} \tag{3.4}$$

(Hibbeler, 106).

Creep is the slow, permanent deformation which occurs when a material is

subjected to stresses and/ or high temperatures for a long period of time.

The rate at which creep occurs is generally increases with applied stress

and/ or temperature (Hibbeler, 109).

3.2   APPLICATIONS OF HYDROGELS

In the natural world, gels play important roles in many fluidic systems.

For instance, in mammalian bodies, the cornea, vitreous, connective tissues,

stomach lining, pulmonary lining, blood vessel membranes, and kidney

membranes (to name a few) are all gels. Gels are natural containers for fluid.

Unlike cells, which set up a boundary between fluid (in many cases, water) and

the environment, gels capture fluid in the spaces within the network of the gel.

Gels thereby allow fluids to maintain particular shapes by dispersing the fluid

throughout the network (Tanaka, 1-2).

These applications in the natural world have inspired many material

applications, especially with hydrogels. As stated in the previous section,

hydrogels have high water contents and are rubbery, making them the logical

substitutes for natural gels. Accordingly, hydrogels have been applied as artificial

biological tissues (Hilt *et al.*, 2003), such as artificial vitreous (Tanaka, 1-2), as

well as soft contact lenses, plastic surgery implants (Tanaka, 1-2), sutures, and

dental implants (Hilt *et al.*, 2003). In addition, gels absorb large volumes of fluid in disposable diapers and sanitary napkins and maintain moisture levels when used as wrappings for meat and fish (Tanaka, 1-2).

3.2.1   MICROFLUIDIC SENSORS AND ACTUATORS

Hydrogels are particularly attractive materials for sensors and actuators in microelectromechanical systems (MEMS) because their sensitivity to environmental factors can be adjusted. By including specific functional groups on the backbone of each polymer molecule later crosslinked to form a hydrogel, the hydrogel can be made sensitive to particular environmental factors, including temperature, pH, electric field, and ionic strength (Hilt *et al.*, 2003). For instance, the hydrogel poly (methacrylic acid) (PMAA), which is sensitive to changes in pH, can be polymerized directly onto a silicon microcantilever in a user-controllable design. When this microcantilever was exposed to solutions of varying pH, the hydrogel swelled or deswelled from its initial equilibrium state depending on the pH of the system. When the hydrogel swelled, it bent the microcantilever. Within a few minutes, the hydrogel equilibriated, and this final curvature could be measured from the deflection of a laser directed at the exposed end of the microcantilever, relative to its position in the initial swelled state. This system demonstrated that the hydrogel could sense and quickly react to environmental changes and was, therefore, ideal for MEMS components (Hilt *et al.*, 2003).

3.2.2 CONTROLLED DRUG DELIVERY DEVICES

In general, polymers are attractive materials for innovative controlled drug delivery systems. Like conventional drug delivery systems, controlled drug delivery systems transport drugs into the body. Controlled drug delivery systems, however, provides a means by which the location and time interval during which the drug is released can be controlled and thereby provides opportunities to target specific cells and locations. Extensive research has revealed that polymers offer great promise in a variety of drug delivery systems and especially controlled drug delivery systems. Conventionally, polymers served merely as containers for drugs, but in newer polymer therapeutics, the polymer is actually conjugated to the drug in many cases and, thus, plays a more active role in the delivery of the drug than before. Moreover, the characteristics of polymer therapeutics can be customized during polymer synthesis, offering great control and precision. Already, some polymer-protein conjugates have been approved for the market, and polymer-anticancer-drug conjugates are undergoing clinical trials (Duncan, 2003).

Due to the similarity of hydrogels to biological tissues and the ability to tailor the properties of the hydrogel to meet the needs of the system, hydrogels are of interest for controlled drug delivery devices. For instance, the hydrogel in this study, PNIPAm, has been investigated because of its sensitivity to temperature. At temperatures close to the physiological temperature (37ºC), the hydrogel

undergoes a phase separation so that any drug contained within the hydrogel will be released into the environment. Moreover, the temperature at which PNIPAm undergoes the phase separation can be tailored with chemistry with relative ease and precision. All of these features make PNIPAm an excellent material for controlled drug delivery systems (Eeckman *et al.*, 2004).

All of these applications require an extensive knowledge of the mechanical properties of hydrogels and an effective and accurate technique to determine those material properties. To satisfy the latter requirement, an accurate mechanical model is needed.

3.3   BRIEF INTRODUCTION TO MECHANICAL MODELS

Although the study of mechanics can be traced back to the experiments of Galileo (Hibbeler, 4), the systematic description of the stresses and strains resulting from contact between two surfaces truly began with the work of Hertz in 1880. Hertz was studying Newton's optical interference rings produced between two glass lenses in contact with one another (Johnson, 90). Wondering if the deformation of the lenses resulting from the contact affected the interference pattern, Hertz assumed that the contact area could be considered elliptical. For continuous contact in the contact area and for boundaries far enough from the contact area so that edge effects were negligible, he calculated that the radius of the contact area, a, was related to the radius of the indenter tip, R, and the total load, P, by

$$a^3 = \frac{6R}{8E_r}P \tag{3.5}$$

where E_r is the reduced modulus given by

$$\frac{1}{E_r} = \left[\left(\frac{1 - v_s^2}{E_s}\right) + \left(\frac{1 - v_i^2}{E_i}\right)\right] \tag{3.6}$$

E_s is the Young's modulus of the hydrogel film, and v_s is Poisson's ratio of the hydrogel film. Similarly, E_i is the Young's modulus of the indenter, and v_i is Poisson's ratio of the indenter (Johnson, 90-93).

The Hertz model does not accurately describe thin films of hydrogels. The Hertz model assumes ideal elastic materials, whereas hydrogels are not only viscoelastic but also poroelastic. In addition, the Hertz model does not account for the adhesion between the indenter and the film, which is evident in these experiments (see Chapter 6 for Results) and which has been demonstrated to have a significant impact on the calculated contact area (and therefore elastic moduli) (Carrillo *et al.*, 2005; Johnson *et al.*, 1971).

The next major contact model relevant to this study was completed by Oliver and Pharr. Oliver and Pharr were studying the mechanical models needed to extract the mechanical properties of stiff materials – such as tungsten, fused silica, and quartz – from force-displacement data collected using an indenter. Similar to my indentation measurements with an atomic force microscope (AFM), Oliver and Pharr used an indenter to indent a stiff material sample and record the force and resulting displacement of the indenter into the sample. The Oliver and Pharr model improves on previous models by accounting for the nonlinear

unloading curve. The Oliver and Pharr model found that the following

relationship between the total load (P) and the total deformation of the material

(h) best described the experimental data:

$$P = A(h - h_f)^m \tag{3.7}$$

where A, m, and h_f are constants that are determined by a fit of the experimental

data with the method of least squares (Oliver *et al.*, 1992).

Like the Hertz model, the Oliver and Pharr model does not accurately

describe hydrogel thin films. The Oliver and Pharr model was developed for

materials that displayed elastic and plastic deformation but does not account for

the viscoelastic and poroelastic behavior of hydrogels. Moreover, the Oliver and

Pharr assumes that the material deforms plastically for the first few indents but

then displays elastic deformation. In other words, the material retains a certain

indent resulting from the first few indentations (Oliver *et al.*, 1992). Hydrogels,

however, are elastic materials and recover completely from deformations.

Finally, the Oliver and Pharr model assumes adhesion is negligible (Oliver *et al.*,

1992), which is clearly an inaccurate assumption in hydrogel indentation

measurements (see Chapter 6, Results). Consequently, the contact area in the

Oliver and Pharr model is smaller than the actual area, leading to overestimation

of elastic moduli (Carrillo *et al.*, 2005).

The hydrogels are most accurately described by one of three models which

account for adhesion. The three models which account for adhesion are the

Johnson-Kendall-Roberts (JKR), Maugis (or Maugis-Dugdale), and Derjaguin-

Muller-Toporov (DMT) models, and each model applies to different contact

characteristics. The JKR model applies to contacts in which a sample of high

surface energy and small elastic moduli (more pliable) is indented with a tip with

a large radius of curvature. The DMT model applies in the opposite contact

conditions (i.e., large elastic moduli (more rigid) and low surface energy materials

indented with a tip with a small radius of curvature). In between these two

conditions, the Maugis model applies. The exact contact conditions and the

appropriate model to calculate the mechanical properties of the system are

determined using the Tabor parameter, a dimensionless number represented here

as μ, which can be calculated using the formula:

$$\mu = \left(\frac{RW_A^2}{E_r^2 z_0^3}\right)^{\frac{1}{3}} \tag{3.8}$$

where R is the radius of curvature of the tip, W_A is the thermodynamic work of

adhesion per unit of contact area, E_r is the reduced modulus of the sample, and z_0

is the equilibrium separation of the surfaces in the Lennard Jones potential. E_r is

given by each model. For instance, in a simple fit of the JKR model to

experimental data, E_r is given by

$$E_r = \frac{-3P_{adh}}{\sqrt{R}}\left[\frac{3(\delta_0 - \delta_{adh})}{1 + 4^{-\frac{2}{3}}}\right]^{-\frac{3}{2}} \tag{3.9}$$

δ_0 is the displacement where the load is zero on the unloading curve. δ_{adh} is the

displacement at the minimum of the unloading curve. P_{adh} is the force at the

minimum of the unloading curve, and R is the radius of the tip (Ebenstein, 2011).

When the Tabor parameter is less than 0.1, the DMT model is appropriate. When the Tabor parameter is greater than 5, the JKR model applies (Carrillo *et al.*, 2005). In the range between 0.1 and 5, Maugis model applies (Ebenstein, 2011).

These mechanical models relate the force-displacment data collected with AFM to the mechanical properties of the materials. In this study, I use AFM to measure the response of photocrosslinkable hydrogels to a range contact conditions, from varying loads to varying loading rates (velocities). Each mechanical model describes the response expected from a material with a particular set of mechanical properties. These models thereby provide the means to correlate the response observed with the mechanical properties that produce such a response. Selecting or even formulating a model which accurately describes a material's response to deformation is absolutely critical to accurate determination of mechanical properties.

3.4   MOTIVATION AND OBJECTIVES OF MY WORK

Hydrogel thin films have applications in a variety of nanoscale systems. For example, because hydrogels are sensitive to environmental conditions such as pH and temperature, they are ideal materials to be used as microfluidic sensors and actuators, such as those used in the lab-on-a-chip devices being developed to diagnose diseases cheaply and swiftly especially in areas without access to a larger scientific laboratory (Bashir *et al.*, 2002). Furthermore, because of hydrogel's resemblance to natural biological tissues and environmental

sensitivity, hydrogels are ideal controlled drug delivery devices (Hilt *et al.*, 2003). Since PNIPAm is thermosensitive, it is particularly well-suited for application as controlled drug delivery devices (Eeckman *et al.*, 2004). To design and optimize these applications, the mechanical properties of PNIPAm thin films should be extensively investigated. Although the mechanical properties of PNIPAm have been extensively investigated, photo-crosslinkable PNIPAm has not been thoroughly studied. Photo-crosslinking offers a safer, more sensitive method to control the crosslinking density and to pattern microscale features in hydrogel thin films. This microscale precision and control make photo-crosslinking an attractive technique for a variety of microscale hydrogel applications. Therefore, this study seeks to understand how the photocrosslinking affects the mechanical properties of PNIPAm thin films.

This research was also motivated by my work with Professor Hayward at University of Massachusetts Amherst in the summer of 2010. In that research project, I worked to develop a novel mechanical characterization method for PNIPAm thin films. Although the flexibility and high water content of hydrogels make them ideal materials for microfluidic sensors and controlled drug delivery devices, these properties make conventional characterization techniques challenging. In the characterization technique which I investigated that summer, a thin hydrogel film was attached to a well-characterized polymer substrate. This bilayer was released from the substrate to form a free-floating bilayer in solution, and the solution simultaneously stimulated the hydrogel to swell, resulting in

curvature of the sample. The Young's modulus of the hydrogel could then be measured via simple, visual interpretation of the sample's curvature (versus depth-sensing indentation (DSI)). My research determined viable substrates and investigated adherence complications. These challenges prompted us to investigate the mechanical properties of photo-crosslinkable hydrogel films further to determine the optimal conditions for this mechanical characterization technique. Eventually, we hope to use the data from this AFM study to validate this curvature technique.

This research employs DSI (performed with AFM) to investigate the mechanical properties of photo-crosslinkable PNIPAm thin films. The AFM is used to collect force-displacement curves, and mechanical models must then be used to calculate the mechanical properties from that data. The available mechanical models described briefly in section 3.4 and discussed in depth in chapter 4. Previous work suggests that the JKR model is the most appropriate model, given the physical parameters of the experimental system (Carrillo *et al.*, 2005; Ebenstein, 2011). The JKR model, however, does not account explicitly for viscoelastic or poroelastic behavior, both of which PNIPAm films exhibit. My research, therefore, seeks to understand under what conditions the JKR model accurately describes even this viscoelastic and poroelastic system and to alter the model as needed to account for the viscoelasticity and poroelasticity of PNIPAm and other polymer thin films.

In summary, my primary objectives for this research are to answer the

following questions:

1. How does photocrosslinking affect the mechanical properties of PNIPAm copolymer thin films?

2. Under what conditions does the JKR model accurately describe the mechanical behavior of PNIPAm copolymer thin films?

3. How should the JKR model be altered to account for the viscoelastic and poroelastic behavior?

3.5 OVERVIEW OF MY WORK

In this research, PNIPAm thin films were photo-crosslinked and then indented using an AFM at varying velocities to understand the effects of viscoelasticity and poroelasticity on the behavior of thin films. The resulting force-displacement data and known physical properties of the film were used to determine the most appropriate mechanical model that described the system and the conditions in which that model was most accurate. This model was then used to calculate the Young's moduli of the PNIPAm copolymer thin films at various velocities. In addition, the force-displacement data were used to understand the viscoelastic and poroelastic relaxation behavior of the PNIPAm thin films.

4. MECHANICAL CHARACTERIZATION TECHNIQUES AND MECHANICAL MODELS

OVERVIEW

In this chapter, I will summarize the different mechanical characterization techniques and then describe different mechanical models. In particular, I will introduce the Hertz model, which founded contact mechanics and which provides the basis for all future mechanical models. Next, I will introduce Oliver and Pharr model, the Derjaguin-Muller-Toporov (DMT) model, the Maguis model, and the Johnson-Kendal-Roberts (JKR) model, the primary model used in this study. Each model accounts for a certain range of mechanical characteristics, and the Tabor parameter is used to determine the most appropriate model for the experimental system. In our experiments, the most appropriate model is the JKR model, which accounts for the significant adhesion seen in our measurements and for the relatively small Young's moduli of the hydrogels.

4.1 RHEOLOGY

Rheology is defined as the study of the deformation and flow of materials. This field includes two major categories of study: solid mechanics and fluid mechanics. In solid mechanics, the dominant behavior is elasticity, which can be described by Hooke's Law for small strains. Hooke's Law states that the applied

stress s is proportional to the strain γ, where the constant of proportionality is

known as Young's modulus of elasticity E:

$$s = E\gamma \tag{4.1}$$

In fluid mechanics, the dominant behavior is viscosity, where the flow is

described by Newton's Law for small changes in the rate of strain:

$$s = \eta \frac{d\gamma}{dt} \tag{4.2}$$

where s is the applied stress, η is the viscosity, and γ is the strain (Carraher, 373-

374).

Conventional rheology employs three basic physical tests to determine the

relationship between stress and strain for the material. The test in Figure 4.1.1(a)

is the compressive stress rheological test, where compressive stress is applied to

the sample. The test in Figure 4.1.1(b) is the tensile stress rheological tests, where

tensile (pulling stress) is applied to the sample. Finally, the test in Figure 4.1.1(c)

is the shear stress rheological test, where one edge of the sample is twisted in one

direction concurrent with the opposite surface of the sample is twisted in the

opposite direction (Carraher, 380).
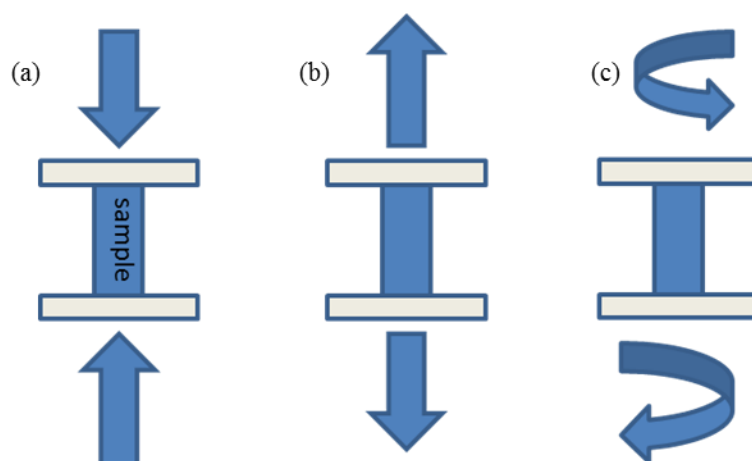
Figure 4.1. 1: The conventional rheological tests: (a) compression test (Carraher, 380); (b) tensile test; (c) shear test (Cowie *et al.,* 350)

These tests, however, are not ideal for hydrogel thin films like those investigated in this research. First, these classic physical tests require macroscopic samples, but the systems I am investigating are nanoscale and are being investigated for their eventual application in nanoscale systems such as nanoscale controlled drug delivery devices and microfluidic actuators. Second, rheology requires homogeneous samples in order to characterize the material accurately. The mechanical properties of soft and anisotropic samples, however, such as hydrogels may be heterogeneous, especially in macroscopic samples (Carrillo *et al.*, 2005). Third, these physical tests require friction to be effective, but the high water content of hydrogels reduces the friction. Fourth, a discrepancy exists between the macroscopic properties measured using these classical rheological tests and those measured using depth-sensing indentation (Kranenburg *et al.*, 2009). Because hydrogel thin films are investigated for eventual application in nanoscale systems, we need to measure the nanoscale

properties. In summary, we need a technique to measure the nanoscale properties, for which purpose depth-sensing indentation is preferable (see next section).

4.2 DEPTH-SENSING INDENTATION

Depth-sensing indentation (DSI) is a mechanical characterization technique particularly well-suited for nanoscale samples such as hydrogel thin films. In DSI – also known as instrumented indentation, load and depth-sensing indentation, microindentation, nanoindentation, and ultra-microindentation – a rigid probe is indented into the material being characterized, and the indentation depth of the probe into the material is recorded as a function of the force applied to indent the material. This data, along with the geometry and mechanical properties of the indenter, are used to calculate the material constants, including the Young's modulus, using mechanical models (Kranenburg *et al.*, 2009) (see section 3.4 for a brief introduction to mechanical models and chapter 4.4 for an in-depth discussion).

DSI is an attractive technique for thin polymeric films because the technique requires only a small volume of sample, which is especially appealing for expensive materials or a limited supply of the materials. Moreover, the thin films can be indented on any available surface of the film. Indentation measurements can be used to measure the mechanical properties as well as gradients of material properties (Kranenburg *et al.*, 2009). Furthermore, DSI can probe local mechanical properties in inhomogeneous (either topography or

properties) samples, such as biological samples or hydrogels (Ebenstein, 2011).

In all of my experiments, I am indenting the hydrogel thin film with forces less than 100 micronewtons (usually 1.00 μN or 1.50 μN), in which case DSI is known as microindentation. Consequently, I will henceforth use the term microindentation to describe DSI in my experiments.

4.3 ATOMIC FORCE MICROSCOPY

Atomic force microscopy (AFM) is a widely-used instrument well-adapted to perform micro- or nanoindentation experiments. In the DSI measurements I performed with the AFM, a microscopic probe is brought into contact with the sample (Eaton *et al.*, 9-10). A beam of collimated light is directed onto the reflective back of this probe, and the reflected light hits a photodiode (Eaton *et al.,* 22) that detects the position of the reflected light. As the probe (also known as the tip) indents the sample, the probe bends, changing the deflection of the light on the photodiode (Eaton *et al.,* 35-36), which is previously correlated to the force exerted on the tip (Eaton *et al.,* 42-44). The indentation continues until the deflection reaches the maximum force that the user specifies. The tip then retracts. Throughout this process, the indentation of the tip and corresponding force exerted on the probe are recoded simultaneously, producing a force-displacement curve (also known as a force curve) (Eaton *et al.,* 35-36).

A typical force curve for my measurements is shown in Figure 4.4.1. The red curve corresponds to the measurements of force and indentation when the tip

is being extended to contact the sample. The tip contacts the sample at the point

where the slope of the red curve dramatically increases. At the peak where the

red and blue curves meet, the AFM applies the user-specified maximum force.

Then the blue curve is the retraction of the tip from the sample. In samples

without adhesion, the extension (red curve in Figure 4.3.1) and retraction (blue

curve in Figure 4.3.1) curves align. The relatively large difference between the

two curves indicates that considerable adhesion is present in these measurements,

which mechanical models need to account for in order to measure accurately the

mechanical properties of the material.
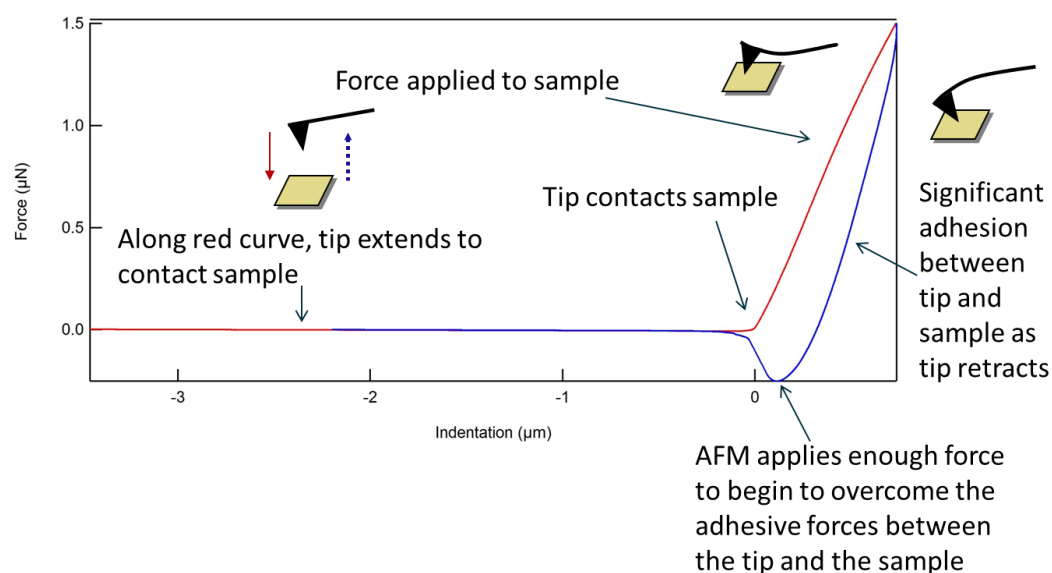
Figure 4.3. 1: A typical force curve seen in these measurements with important features marked.
The red curve is the extension and indentation of the probe into the sample, and the
blue curve is the retraction of the probe from the sample. Significant adhesion can
be seen in this force curve because the blue and red curves do not align.

Although the AFM allows us to construct force curves, we need mechanical

models to interpret the curve and determine the material properties that produce

the measured response.

4.4 MECHANICAL MODELS

4.4.1 INTRODUCTION TO MECHANICAL MODELS

When two bodies come into contact and a force is applied to press the bodies together, the bodies contact over a finite area much smaller than the dimensions of the bodies themselves. A theory of contact, also known as a mechanical model, may then be used to calculate the dimensions of the resulting contact area, the relationship of the load to the size of the contact area, the tractions at the interface (Johnson, 84) – which transmit forces and moments between the bodies (Johnson, 5) – and the stresses and strains both at the interface and within the material immediately surrounding the contact area (Johnson, 84). In the following discussion, the coordinate system in these equations is assumed to have its origin at the first point of contact before loading (see Figure 4.4.2.1(a)). The plane tangent at the point to both contacting surfaces is defined as the x-y plane, and the axis normal to the x-y plane through that origin is the z-axis (Johnson, 2). This coordinate system is shown in Figure 4.4.2.1.

4.4.2 HERTZ

In 1880, Hertz was studying Newton's optical interference rings produced between two glass lenses in contact with one another. Hertz realized that the lenses were elastic materials (Johnson, 90) and, consequently, deformed under the

pressure exerted to maintain the contact between them (Johnson, ix). Concerned about the effects of this deformation on the interference pattern, Hertz formulated the first valid theory of contact over the Christmas holidays (Johnson, 90) and thereby germinated the field of contact mechanics (Johnson, ix).

The Hertz theory describes the stresses and strains for smooth, non-conforming surfaces in contact for both static and quasi-static loading (Johnson, 90). To be smooth, the contact between the surfaces must be continuous within the contact area both microscopically and macroscopically (Johnson, 84). Non-conforming surfaces are surfaces which have distinct profiles and thus do not fit together continuously when brought into contact. For example, the two surfaces shown in Figure 4.4.2.1(a) are non-conforming surfaces (Johnson, 1).
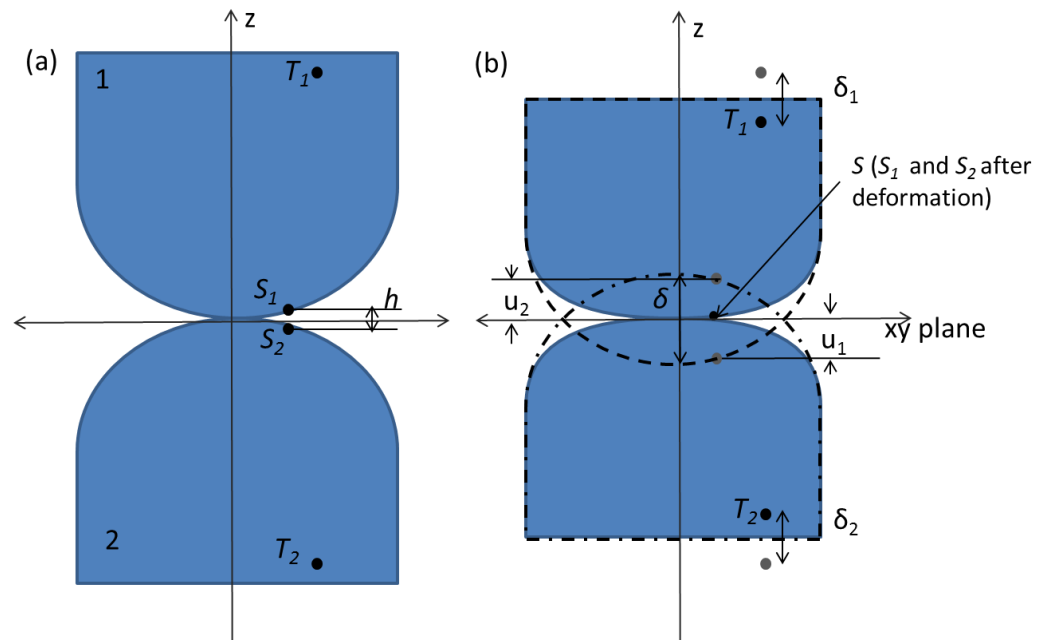
Figure 4.4.2. 1: (a) Bodies 1 and 2 are in contact before a load is applied. h is the separation between points S_1 and S_2 on the surface of body 1 and 2, respectively, but not in contact with each other. (b) Both bodies deform when a load is applied. The dashed line shows the contour of body 1 if it did not deform, and the gray dot shows

the position of S_1 if the body had not deformed. The dashed and dotted line shows the contour of body 2 if it did not deform, and the gray dot shows the location of S_2 if the body had not deformed. The black dot lying in the contact area in the x-y plane shows the position of S_1 and S_2 (now lying on top of each other and labeled a single point S) after the deformation. u_1 is the displacement of point S_1 without deformation, and the same is true for body 2. The gray dots near points T_1 and T_2 indicate the locations of the two points before the bodies deformed. δ_1 and δ_2 are the displacement of T_1 and T_2 after load is applied.

To describe systems such as the one shown in Figure 4.4.2.1, Hertz

simplified the calculations with several assumptions. In Figure 4.4.2.1, two

elliptical paraboloid bodies, which can be considered roughly spherical locally, in

part (a) of Figure 4.4.2.1 are brought close but not quite into contact. In part (b)

of the same figure, the surfaces are brought into contact and loaded. First, for the

Hertz theory to be valid for this system, the contact area must be small compared

to the size of each body. In this case, the contact area and the surfaces just

outside the contact area can be considered planar. Most importantly, the strains

are small enough to be described by the linear theory of elasticity. Second, both

surfaces must be frictionless so that the interaction involves only pressure acting

normal to the planar contact area.   As a result of these assumptions, Hertz could

model each body as a solid with one planar surface but all other dimensions

stretching to infinity where force is applied only in the elliptical contact areas on

each body's surface. The boundaries of the bodies can thus be ignored, and the

contact deformation and distribution of stresses is independent of the system used

to buttress and manipulate each body (Johnson, 91).

Before the two surfaces contact, the contours of the bodies within the

subsequent contact area can be considered elliptical paraboloids with the proper

choice of axes (see Figure 4.4.2.1(a)). Relative to the coordinate systems of each

body, the surfaces can then be described by the following equations, in which the

number 1 and 2 indicate the quantities describing body 1 and 2, respectively:

$$z_1 = \frac{1}{2R_1'}x_1^2 + \frac{1}{2R_1''}y_1^2 \tag{4.3}$$

$$z_2 = -\left(\frac{1}{2R_2'}x_2^2 + \frac{1}{2R_2''}y_2^2\right) \tag{4.4}$$

R' is the minimum principal relative radius of curvature of the surface at the

origin and R'' is the maximum principal relative radius of curvature of the surface

at the origin (Johnson, 85). Now using the common set of axes shown in Figure

4.4.2.1, the separation h between points $S_1(x,y,z_1)$ and $S_2(x,y,z_2)$ which lie on the

surfaces of the respective bodies can be written in terms of R' and R'':

$$h = z_1 - z_2 = \frac{1}{2R'}x^2 + \frac{1}{2R''}y^2 \tag{4.5}$$

Equation 4.5 captures the fact that when an elliptical paraboloid is "sliced"

perpendicular to the z-axis (as defined in Figure 4.4.2.1(a)), the resulting surface

area is elliptical. The separation between two such elliptical slices on which S_1

and S_2 lie is h (Johnson, 85-87).

When two elliptical paraboloid surfaces described by the equations above

are placed under a total normal load P, the surfaces deform (see Figure

4.4.2.1(b)). As shown in Figure 4.4.2.1(b), the two points T_1 and T_2 far from the

origin are displaced by distances δ_1 and δ_2, respectively, in the z-direction as the

load is applied. S_1 and S_2 on the surface of the bodies are displaced until they

contact each other within the contact area and are relabeled as point S. If each body passed through the other under the load, these points would be displaced in the z-direction by distances $\bar{u}_1$ and $\bar{u}_2$. $\bar{u}_1$ and $\bar{u}_2$ depend on material properties (for example, these distances will be smaller for a stiffer material) and are smaller than δ_1 and δ_2. Once the system has reached a new equilibrium, the total motion δ of T_1 and T_2 (where $\delta = \delta_1 + \delta_2$) will be equal to the motion of the two surfaces as they come into contact (h) plus the deformation of the surfaces ($\bar{u}_1$ and $\bar{u}_2$):

$$\bar{u}_1 + \bar{u}_2 + h = \delta \tag{4.6}$$

Substituting our expression for h, we derive an expression for any two points S_1 and S_2 both on the contact surfaces:

$$\bar{u}_1 + \bar{u}_2 = \delta - h = \delta - \frac{1}{2R'}x^2 - \frac{1}{2R''}y^2 \tag{4.7}$$

(Johnson, 88).

Hertz proposed that for two identical solids of revolution (where $R_1' = R_1'' = R_1$ and $R_2' = R_2'' = R_2$ and R is the relative curvature of the surfaces), the pressure that satisfies the conditions above is given in terms of the maximum pressure p_0 by

$$p(r) = p_0 \left\{ 1 - \left(\frac{r}{2}\right)^2 \right\}^{\frac{1}{2}} \tag{4.8}$$

where, if we use a polar coordinate system to describe the contact plane, r is the radial coordinate of the contact plane. The normal displacement within the resulting circular contact area is uniform. For this case:

$$\bar{u}_1 + \bar{u}_2 = \delta - h = \delta - \frac{1}{2R}r^2 \tag{4.9}$$

He then derived that the displacement for both surfaces in the z-direction is given

by

$$\bar{u}_z = \left(\frac{1-v^2}{E}\right)\frac{\pi p_0}{4a}(2a^2 - r^2) \tag{4.10}$$

where a is the total radius of the circular contact area. Applying Newton's Third

Law, the pressure on one surface is equal to the pressure exerted on the other

surface, and we can rewrite the expression for $\bar{u}_1$ and $\bar{u}_2$ as

$$\frac{\pi p_0}{4aE_r}(2a^2 - r^2) = \delta - \left(\frac{1}{2R}\right)r^2 \tag{4.11}$$

where the reduced modulus E_r is given by

$$\frac{1}{E_r} = \frac{1-v_1^2}{E_1} - \frac{1-v_2^2}{E_2} \tag{4.12}$$

The total force applied to make the solids contact is found by integrating the

expression for $p(r)$ to give

$$P = \frac{2}{3}p_0\pi a^2 \tag{4.13}$$

a, δ, and p_0 can be solved for from these equations:

$$a = \left(\frac{3PR}{4E_r}\right)^{\frac{1}{3}} \tag{4.14}$$

$$\delta = \frac{a^2}{R} = \left(\frac{9P^2}{16RE_r^2}\right)^{\frac{1}{3}} \tag{4.15}$$

$$p_0 = \frac{3P}{2\pi a^2} = \left(\frac{6PE_r{}^2}{\pi^3 R^2}\right)^{\frac{1}{3}} \tag{4.16}$$

Although this model provides the basis from which all the other models are developed, it is not appropriate for the thin PNIPAm films investigated in this research. First, the model does not account for the significant adhesion between the probe and the sample in these experiments (see Chapter 7 for my Results). These adhesive forces result in a larger contact radius than the equation above calculate (Carrillo *et al.*, 2005; Johnson *et al.*, 1971). In addition, the adhesive forces change the indentation depth, the size of the air gap outside the contact area between the two surfaces (*h*), and the elastic energy stored in the system (Maugis, 1992). Second, the Hertz model assumes ideal elastic materials, whereas hydrogels are viscoelastic and poroelastic. In summary, a more sophisticated model accounting for these different features of hydrogel films must be used to describe accurately the hydrogel film.

4.4.3 OLIVER AND PHARR

In 1992, Oliver and Pharr published a paper in which they outlined their own mechanical model for indentation measurements utilizing the relationships among indentation, applied force, and area of contact derived by Sneddon. In these relationships, for simple indenter geometries, the applied load P is exponentially related to the elastic indentation of the probe into the sample h (which is different from the h defined in the previous section), where the value of

the exponent is determined by the indenter geometry (Oliver *et al.,* 1992).

Oliver *et al.* used Tabor's experiments investigating the response of metals to indentation. Because the geometry of the impressions formed by the indenter in metal samples is a slightly enlarged version of the indenter geometry, Tabor determined the relationships among the unloading curve, the elastic modulus of the material, the size of the impression in the sample, and the amount of elastic indentation. Moreover, the reduced modulus E_r, as defined equation 4.12 in the previous section, incorporates the influence on the load-displacement curve from non-rigid indentation probes (Oliver *et al.,* 1992).

Oliver *et al.* finally use the stiffness determined from the experimental curves in their analysis. From previous force-displacement measurements, the stiffness S is defined as the change in the load P with indentation h:

$$S = \frac{dP}{dh} = \frac{2}{\sqrt{\pi}} E_r \sqrt{A} \qquad (4.17)$$

In this equation, S is measured from the upper part of the experimental unloading curve, and A is the predicted contact area during elastic deformation. This equation applies for any indenter which can be described as smooth body of revolution and even extends to some that cannot be (Oliver *et al.,* 1992).

Several assumptions were made in the derivation of this analysis method. First, the experimental data supported the approximation of the Berkovich indenter (a pyramidal indenter with three faces) used in the experiments as a conical indenter or paraboloid of revolution since these geometries account for the nonlinear behavior and varying contact area. Second, flat surfaces and surfaces

with residual impressions are both accurately described by Sneddon's relationships, as long as the differences of the geometry of the surface deformation are accounted for. Third, the contact area can be predicted from the area function of the indenter and the vertical component of the indentation because the sample adapts to the indenter geometry. This assumption, however, does not account for adhesion, which is a significant influence on the contact area.

In the Oliver and Pharr model, the stiffness relationship is solved for E_r. A is given by the area function of the indenter in terms of the vertical component of the indentation over which the sample contacts the indenter (the contact depth, h_c). The contact depth is found experimentally using that the relationship among the total indentation h, h_c, and the indentation of the sample at the edges of the contact area h_s:

$$h = h_c + h_s \qquad (4.18)$$

Rewritten in terms of the maximum indentation h_{max}, the relationship becomes

$$h_c = h_{max} - h_s \qquad (4.19)$$

To determine h_s from the experimental data, Sneddon's equations describing the deformation of the surface at the edges of the contact area in terms of the geometry of the probe were used. S is determined by fitting the unloading curve.

Although this model is accurate for indentation measurements on thin films of metals, the Oliver and Pharr model uses the assumption that all adhesive forces are negligible to calculate the contact area using simply the indenter area function and the contact depth. Although this model is valuable for systems

lacking significant adhesion, we must use a different model to calculate the mechanical properties from measurements in this research where we do see considerable adhesion.

4.4.4 DMT

Derjaguin first addressed the effect of adhesive forces on contact area in 1934 when he incorporated adhesive forces into the Hertz model and calculated the full contact area between two contacting surfaces. This analysis, however, was flawed because it accounted for the adhesive forces acting in the circular area surrounding the actual contact area but assumed that those adhesive forces did not change the contact area appreciably (Derjaguin *et al.,* 1975).

Derjaguin and colleagues later improved their model. They consider elastic contact between a spherical, elastic particle with radius *R* and a solid, absolutely-hard planar surface, assuming *R* is relatively small so that surface roughness and small contaminant particles have negligible influence on the contact area calculated. The contact area is assumed to be Hertzian, with the corresponding descriptions of pressure and deformation. The relationship within the radius of the contact area between the vertical deformation of the elastic bead and radial distance from the origin determined in this analysis was then used to calculate the interaction energy, the combination of the energy of the elastic deformation and the energy due to the different forces at the molecular level. Once the interaction energy is known, the adhesive forces between the two

surfaces can be solved for (Derjaguin *et al.,* 1975).

Although the DMT model incorporates the adhesive forces outside the contact area into the description of the system, it assumes that no adhesive forces act within the contact area itself so that the contact area can be described by the Hertz equations (Maugis, 1992). This assumption is not physically realistic, as outlined in section 4.2 of this thesis. Because the contact area is assumed to be Hertzian, the elastic modulus of the particle cannot be too small, for then the adhesive forces between the particle and surface would produce a contact area larger than that predicted by the Hertz model (Derjaguin *et al.,* 1975). The DMT model, therefore, is accurate only for materials with large moduli − whereas hydrogels have relatively small moduli − and for materials that behave elastically within the contact area − whereas hydrogels are viscoelastic and poroelastic (Derjaguin *et al.,* 1975).

The publication of this research in 1975 sparked a fierce debate through the pages of the *Journal of Colloid and Interface Science.* Tabor highlighted that the original DMT model did not account for the deformation as a result of the adhesive forces at the boundaries of the contact area. When the DMT model was reformulated, the assumption of a Hertzian contact area was abandoned, and the resulting model became one of three used to describe various experimental setups. The particular model appropriate for the specific experimental setting is determined by the Tabor parameter (Maugis, 1992), as described in section 4.4.7.

4.4.5 MAUGIS

In 1992, Maugis published a model utilizing Dugdale analysis to transition smoothly from the DMT model (revised from its original form as noted at the end of the section 4.4.4) to the JKR model (discussed in section 4.4.6). For all the models, the stresses, deformation, and pressure distributions were examined for a cylindrically symmetric crack with a radius a in a solid extending to infinity in all directions. First, the equations of JKR and DMT are reformulated using Sneddon's solutions; in the case of JKR, this reformulation clarifies how and where adhesive forces act and that the JKR model acts within the constraints of the general theory of linear elasticity. Next, Maugis uses the Lowengrub and Sneddon equations to derive a new model describing the elastic displacement of material around but not at the surface of the crack and the distribution of cylindrically symmetric pressure. These equations are then modified to account for the eventual self-equilibration of forces in the solid (Maugis, 1992).

A Dugdale model is then applied to this system of equations. In this model, the stresses are taken to be the same on a length d, equal to the distance between c and a. In addition, the energy release rate is equal to the product of the deformation of the crack opening and the stress on the crack. By examining the - two extremes of the model, Maugis finds that as the ratio of c and a tends to 1 (or c and a become equal), the JKR pressures, stresses, displacements, and energy release rate can be derived. As that ratio tends to infinity, the DMT relations can be derived (Maugis, 1992).

Although the Tabor parameter indicates that the Maugis model is not appropriate for the experimental systems probed in this study, the Maugis model shows that the JKR and DMT models are both accurate in limiting cases and are related. The dimensionless Tabor parameter indicates the appropriate model for a given experimental system (Maugis, 1992).

4.4.6 JKR

The Johnson-Kendall-Roberts (JKR) model was used in this research to extract the mechanical properties of the hydrogel thin films. First, by considering the surface energy, this model specifically accounts for the attractive forces between the tip and sample (Johnson *et al.,* 1971), which are generally significant in the experimental results presented in this thesis. Second, this model accurately describes any system consisting of an elastic, flexible material, a tip with a relatively large radius, and large surface energy (Ebenstein *et al.*, 2006), conditions satisfied by the hydrogel thin films investigated in this thesis.

Surface forces are forces which attract two nearby surfaces toward each other and thereby produce surface energy – energy expended to create a unit contact area between two solids in contact – associated with each surface. When two smooth, solid surfaces contact but are not loaded, the distribution of elastic forces within the solids normally dominates the equilibrium of contact. When a small force is applied to the contact bodies, the surface forces rather than the distribution of elastic forces within the solids exert considerable influence on the

equilibrium. The paper published by Johnson, Kendall, and Roberts in 1971

presents calculations of the mechanical properties of contacting spheres with

significant adhesion through considerations of the surface energy (Johnson *et al.*,

1971).

For two spheres in contact, the total energy (U_T) is the sum of the stored

elastic energy (U_E) and the mechanical energy from the force applied to the

spheres (U_M) and, when surface forces are present, the surface energy (U_s).

Equilibrium is reached when the total energy is constant everywhere within the

contact area. In the Hertz model (where surface forces are absent), the contact

radius a_0 is related to the radii of the two spheres (R_1 and R_2), the applied force

(P_0), and the reduced modulus (E_r) by

$$a_0^3 = \frac{3}{4} \frac{R_1 R_2}{R_1 + R_2} \frac{P_0}{E_r}{}_0 = \frac{3}{4} \frac{R P_0}{E_r} \tag{4.20}$$

But when surface forces act, the contact radius in equilibrium (a_1) is greater than

the radius predicted by the Hertz model (a_0). The load predicted by the Hertz

model for a_1 is obviously larger than P_0 so that

$$a_1^3 = \frac{3}{4} \frac{R P_1}{E_r} \tag{4.21}$$

The elastic energy is the difference between the energy needed to apply load P_1 to

produce a contact area of radius a_1 and the energy released when the load is

decreased to P_0 while maintaining the contact radius a_1. The first energy is

calculated as if the surface forces were not present. But the influence of the

surface forces are incorporated into the second term by the force-displacement

relationship given below:

$$\delta = \frac{2}{3\pi} \frac{PE_r}{a_1}$$

(4.22)

The surface energy U_s is equal to

$$U_s = -\gamma \pi a_1^2$$

(4.23)

Here, γ is the adhesion energy for both surfaces. For the total energy to be stable

at equilibrium Johnson and colleagues determine that

$$P_1 = P_0 + 3\gamma\pi R + \sqrt{6\gamma\pi R P_0 + (3\gamma\pi R)^2}$$

(4.24)

and

$$a^3 = \frac{R}{K}\left(P + 3\gamma\pi R + \sqrt{6\gamma\pi R P + (3\gamma\pi R)^2}\right)$$

(4.25)

The spheres will separate when

$$P = -\frac{3}{2}\gamma\pi R$$

(4.26)

Johnson and colleagues note that the stress distribution used in this analysis leads

to infinite stresses at the boundaries of the contact area, which a physical system

cannot maintain. However, the error introduced because the edges separate

slightly is negligible (Johnson *et al.*, 1975).

4.4.7 TABOR PARAMETER

The Tabor parameter, proposed by Tabor in 1977 in a footnote of a paper,

is the dimensionless number by which we determine whether we are in the regime

described by the DMT, Maugis, or JKR model. It is the ratio of the deformation

of the material when the two surfaces are at the atomic equilibrium separation and the atomic equilibrium separation (Tabor, 1977).

The DMT and JKR descriptions of contacting bodies are first compared. Tabor notes that the DMT model predicts that the surface of the deformable sphere in the ring of area surrounding the subsequent contact area is attracted to the undeformable flat surface, resulting in a general flattening of the sphere's surface as it approaches the flat surface, as shown in Figure 4.4.7.1. This model assumes that no attractive forces act within the contact area itself. In contrast, the JKR model assumes that the attractive forces act primarily within the top several atomic layers (and are, therefore, surface forces) within the subsequent contact area. In comparison, the attractive forces outside the subsequent contact area are negligible. As a result, the surface of the sphere within the contact area is strongly attracted to the flat surface, and the spherical surface in that region deforms toward the flat surface, producing a "necking" behavior, as shown in Figure 4.4.7.2.

D. TABOR
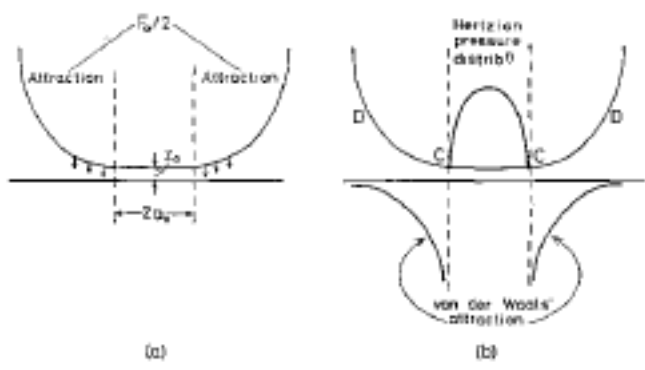
FIG. 5. Interaction between an elastic sphere and a hard flat surface according to Derjaguin *et al.* (10). (a) When the applied normal load is zero, the attractive forces produce a finite circle of contact of diameter $2a_0$. There is repulsion over this area and attraction in the annular region outside. (b) The pressure distribution implied in the Derjaguin analysis (schematic).

Figure 4.4.7. 1: Behavior described by the DMT model (Tabor, 1976)
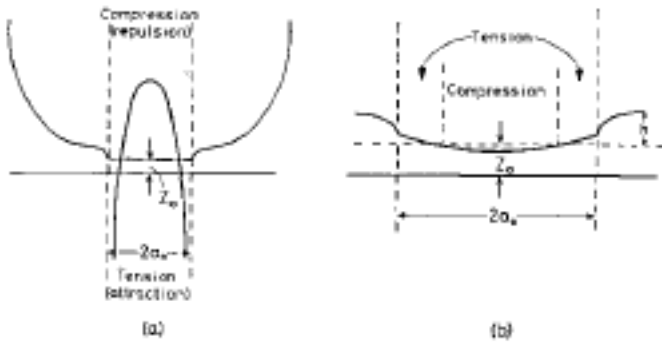
FIG. 6. Interaction between an elastic sphere and a hard flat surface according to Johnson *et al.*; (a) when the applied load is zero, the attractive forces produce a finite circle of contact of diameter $2a_0$. The central region is under compression, the peripheral region under tension. It is assumed that outside the circle of contact the interfacial forces are negligible. (b) Exaggerated features of the contact zone.

Figure 4.4.7.2 : Behavior described by the JKR model (Tabor, 1976).

Tabor studied the air gap between mica sheets with a thickness of several

microns and compared the different theorems. These sheets were glued to glass

cylinders so that the system was equivalent to a sphere contacting a flat surface

and studied this system with a combination of multibeam interferometry

(angstrom resolution) and optical microscopy (micron resolution). All the behavior was assumed to be linearly elastic. Based on the results, Tabor noted that when the surfaces were at atomic equilibrium separation, the assumption that the forces outside the contact zone are negligible is valid only when the height of the "neck" formed as the sphere's surface is attracted to the flat surface is much greater than the atomic equilibrium separation (z_0). Since the height of the neck (h) is proportional to the cube root of the radius of the sphere (R) and the square of the surface energy (W_a) and indirectly proportional to the cube root of the square of the elastic modulus (later shown to be the reduced modulus (E_r), the ratio of the height of the neck to the atomic equilibrium separation is

$$\frac{h}{z_0} = \left(\frac{RW_A^2}{E_r^2 z_0^3}\right)^{\frac{1}{3}} \tag{4.27}$$

To summarize Tabor's findings, when this ratio is large, the "necking" of the sphere is large, and the attractive forces outside the contact area can be neglected. As a result, the JKR model is most appropriate. When this ratio is small, the "necking" of the sphere is negligible, and instead the attractive forces outside the contact area are the dominant influence of the contact area. Consequently, the DMT model is most accurate in this regime (Tabor, 1977).

The accepted value where the DMT model is appropriate is when this ratio, later relabeled μ, is less than 0.1. The JKR model is appropriate when μ is greater than 5. The Maugis model is appropriate when μ is between 0.1 and 5 (Ebenstein, 2011).

5. PREVIOUS WORK ON MECHANICAL CHARACTERIZATION OF

HYDROGELS

OVERVIEW

This section highlights the previous studies of nanoindentation of hydrogels most relevant to this research. Specifically, I will summarize the findings of Carrillo *et al.* (2005); Ebenstein (2011); Junk *et al.* (2010); Cai *et al.* (2010); and Hu *et al.* (2011). Carrillo *et al.* performed nanoindentation measurements on polydimethylsiloxane thin films with different crosslinking densities and calculated the elastic moduli of the film using a range of different models. These moduli were then compared among the different models and to moduli calculated from traditional rheological tests, and the relative merits of the models were discussed (Carrillo *et al.*, 2005). This work helps us to understand why the Johnson-Kendall-Roberts (JKR) model is most appropriate for the hydrogel films in this discussion. Ebenstein developed a simpler method to apply the JKR model, the most relevant model to our research, to nanoindentation measurements to extract the Young's modulus of the films (Ebenstein, 2011). Junk *et al.* studied the temperature dependence of the different mechanical properties of thin films of photo-crosslinkable PNIPAm. This temperature study is one of the best such studies on PNIPAm, and a variety of detailed observations may be relevant to interpreting our data (Junk *et al.,* 2010). Cai *et al.* and Hu *et al.* probed the

poroelasticity of the hydrogel films (Cai *et al.,* 2010; Hu *et al.,* 2011), the effects of which are present in our research.

5.1 F. CARRILLO, S. GUPTA, M. BALOOCH, S.J. MARSHALL, G.W. MARSHALL, L. PRUITT, AND C.M. PUTTLITZ. **20**, *J. MATER. RES.,* 2820-2830, 2005.

Carrillo *et al.* conducted a comprehensive study of the mechanical properties of polydimethylsiloxane (PDMS) hydrogels in both dry and aqueous conditions and compared the elastic moduli calculated using a range of different models as well as conventional rheological measurements. Three samples for each of five different ratios of base to cross-linker agent were prepared, resulting in samples with a range of different crosslinking densities and thus different Young's moduli. First, traditional, rheological compression measurements were performed to provide a baseline measurement with which to compare the nanoindentation results. The elastic modulus was calculated from its definition as the ratio of stress to strain with the assumption that the two are linearly related, resulting in a mean elastic moduli which increased as the crosslink density increased (ranging from 2.04 ± 0.06 MPa for the most crosslinked gel to 0.42 ± 0.05 MPa for the least crosslinked gel). The greater number of crosslinks in the material at these smaller ratios holds the material more firmly in one shape and can more successfully resist deformation.

Carrillo *et al.* next performed nanoindentation measurements and

calculated the Young's modulus for each crosslinking density using the Hertz model, the Oliver and Pharr model, and the JKR model. Nanoindentation with a conospherical probe was performed at a rate of 10 µN/s to a peak load of 100 µN and a maximum indentation depth of 5 µm. The tip was held at this maximum indentation for 10 seconds, and the tip was retracted at the same rate as the approach, resulting in a measurement lasting a total of 30 seconds. In addition to the force-displacement curve, the force needed to overcome adhesion between the tip and the sample (the pull-off force) was recorded.

Figure 5.1.1 compares the mean values of the Young's modulus (*E*) calculated with various models measured in a dry environment. Figure 5.1.2 shows the mean values of the Young's modulus calculated with various models measured in an aqueous environment.
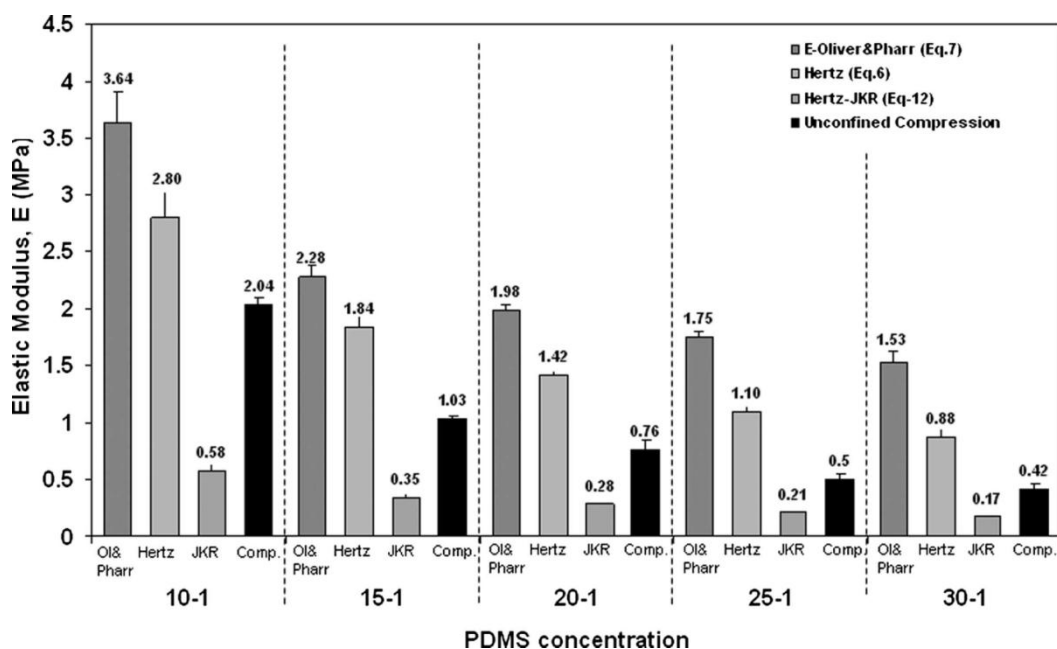
Figure 5.1. 1: Comparison of Young's moduli calculated with various models and at various base to cross-linking agent ratios measured in a dry environment. The stiffest material has the smallest base to cross-linking agent ratio (Carrillo *et al.*, 2005).
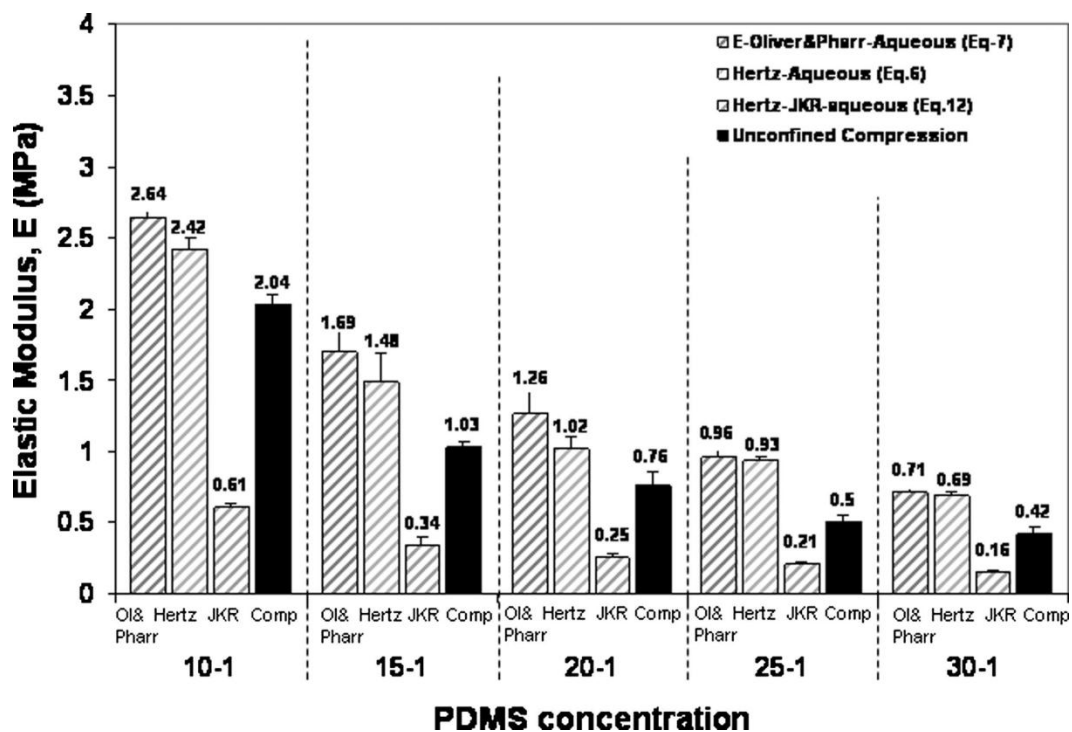
Figure 5.1. 2: Comparison of the Young's moduli calculated with various models for various experimental conditions measured in an aqueous environment. The stiffest material has the smallest base to cross-linking agent ratio (Carrillo *et al.,* 2005)

As shown in Figures 5.1.1 and 5.1.2, for both the Hertz and Oliver and Pharr models, the Young's moduli of the samples indented in an aqueous environment were dramatically smaller than the Young's moduli of samples indented in a dry environment. Generally in nanoindentation measurements, significant adhesion forces were measured and were larger in the dry environment than in the wet environment. In water, the electrostatic charges were weakened, resulting in reduced adhesive forces. Moreover, less crosslinked samples tended to exhibit smaller adhesive forces on the tip than more crosslinked samples, but the adhesive forces were not negligible in any of the samples. Since neither the Hertz nor the Oliver and Pharr model accounts for adhesion, the decrease in the

Young's moduli is probably due to the decrease in adhesive force because measurements in the wet environment are closer to the conditions for which the models were formulated where the adhesive forces are negligible.

Two other features of Figures 5.1.1 and 5.1.2 should be highlighted. First, the elastic moduli calculated using the JKR model do not vary much between dry and aqueous measurement conditions. Second, the elastic moduli for the JKR model are substantially smaller than the corresponding values for the other two models. These two features are probably because the JKR model accounts for the effects of the adhesive forces on the indent depth. These results indicate that adhesive forces must be accounted for in indentation measurements of compliant materials like PNIPAm and suggest that the application of either the Hertz or the Oliver and Pharr model is incorrect for compliant hydrogels because each model assumes negligible adhesive forces (Carrillo *et al.*, 2005). Thus, finding the appropriate model to describe an experimental system is very important.

Although the elastic moduli values obtained from JKR analysis were much less than values from the Hertz and Oliver and Pharr models, Tabor's parameter (see section 3.4 for a brief discussion or section 4.4.7 for more in-depth discussion of this parameter) indicates that the JKR model is the appropriate model for this system. The Tabor parameter is a dimensionless parameter μ calculated using the formula:

$$\mu = \left(\frac{RW_A^2}{E_r^2 z_0^3}\right)^{\frac{1}{3}} \tag{5.1}$$

Here, R is the radius of curvature of the tip, and W_A is the thermodynamic work of adhesion per unit of contact area or the work necessary to pull the tip tip from contact with the substrate to infinity (Carrillo *et al.*, 2005). E_r is the reduced modulus of the sample (see equation 4.12 in section 4.4.2), and z_0 is the equilibrium separation of the surfaces in the Lennard Jones potential. When the Tabor parameter is greater than 5, the JKR model applies. The calculations of the Tabor parameter indicated that the JKR model was most appropriate for the compliant hydrogel films that Carrillo *et al.* investigated (Carrillo *et al.*, 2005).

The results of Carrillo *et al.* emphasize the importance of choosing the appropriate model to describe the experimental systems. These results also suggest that the JKR model is most appropriate for the hydrogel thin films investigated in this thesis, which analysis of the Tabor parameter confirms. As summarized in the Chapter 7, we do observe considerable adhesive forces, as Carrillo *et al.* did. Analysis of the Tabor parameter confirms this initial hypothesis formulated from this research.

5.2 EBENSTEIN, D.M. **26**, *J. MATER. RES.*, 1026-1035, 2011.

Ebenstein examined the role of adhesion in nanoindentation more closely by performing similar indentation measurements as Carrillo *et al.* but now adding measurements in detergent, which substantially reduces the adhesive forces.

Ebenstein uses these measurements in detergent as a baseline modulus value with which to compare the modulus values extracted using various methods when substantial adhesion is present. One of those methods includes the two-point (JKR) method (Ebenstein, 2011), which I use in this thesis to calculate all elastic moduli. Moreover, by using the same tip for all measurements and using force curves to detect the surface and determine the adhesive force for each measurement, this study eliminates the potential errors that Carrillo *et al.* encountered when they used the same previously-determined pull-off force for all calculations (Ebenstein, 2011).

Two disks of PDMS hydrogel with different base to cross-link agent ratios were prepared and attached to glass slides. Tips for nanoindentation were constructed by gluing a boro-silicate glass microsphere onto a piece of tungsten wire. The beads used to indent the PDMS sample with the smaller ratio had a nominal radius of curvature of 130 μm, and the beads used to indent the PDMS sample with the larger ratio had a nominal radius of curvature of 94 μm. Each disk was indented in air, in deionized water, and in 8 mM sodium lauryl sulfate detergent in deionized water. The detergent reduced the adhesive forces between the tip and sample and the capillary forces on the indenter and thereby provided a baseline with which to compare the other measurements (Ebenstein, 2011).

Both quasi-static indents (DSI measurements where the tip starts in contact with the surface) and full nanoindentation measurements were performed on the samples. In the nanoindentation experiments, the probe was extended and

retracted at a velocity of 100 nm/s to a maximum indent of 4500 nm for the sample with the smaller ratio and 8000 nm for the sample with the larger ratio. In both cases, the maximum load was greater than 40 μN. Before and between measurements, the probe was retracted far enough from the sample to be out of range of any attractive forces with the sample (Ebenstein, 2011).

The adhesive force was significant for the air and water measurements but negligible in the detergent measurements. In the air and water measurements, the adhesive force was equal to or greater than 20 μN but was generally larger in air than in water. In water, the adhesive forces and work of adhesion during loading were more reduced than the adhesive forces during unloading. Moreover, in air, the force returned to zero at the end of the unloading curve, but in water retained a force of -3 to -10 μN. Since this effect was observed during calibration of the tip in water, it was hypothesized that this residual negative force is due to interactions between the tip and fluid. In contrast, the adhesive force in detergent was less than 1 μN. Thus, the measurements in detergent could be analyzed using the Oliver and Pharr method, which does not account for adhesion, whereas the air and water measurements were analyzed using the JKR model, confirmed by the Tabor parameter (Ebenstein, 2011).

The JKR model can be applied using the two-point method, where only the force and displacement data at two points need be known to calculate the material properties. Specifically, the reduced modulus E_r in this method is given by

$$E_r = \frac{-3P_{adh}}{\sqrt{R}} \left[\frac{3(x_0 - x_{adh})}{1 + 4^{-\frac{2}{3}}} \right]^{-\frac{3}{2}} \tag{5.2}$$

where x_0 is the displacement where the load is zero on the unloading (retraction) curve, x_{adh} is the displacement at the minimum of the unloading curve, P_{adh} is the force at the minimum of the unloading curve, and R is the radius of the tip (Ebenstein, 2011). These points are shown in Figure 5.2.1 on a typical force curve measured in this thesis.
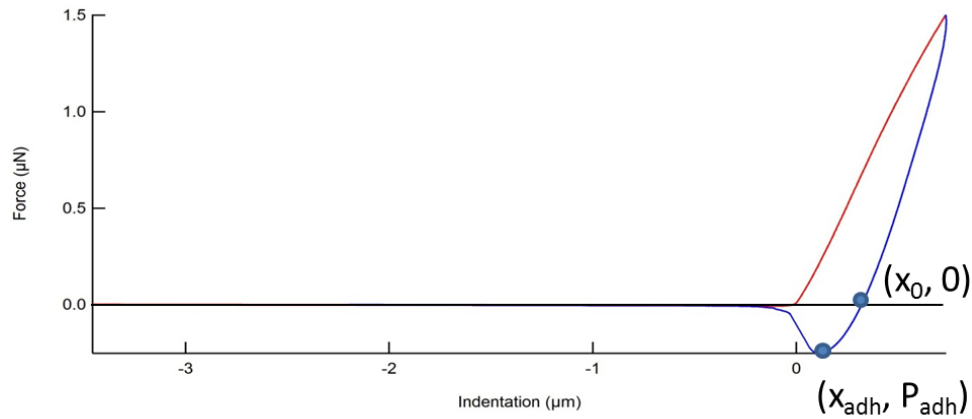
Figure 5.2. 1: Typical force curve with two points used in the two-point method indicated by the blue markers.

This two-point method was used throughout this research to calculate the Young's moduli.

A more rigorous method used by Ebenstein is to fit the unloading curve with the following equation:

$$x - x_{contact} = \frac{a_0^2}{R} \left(\frac{1 + \sqrt{1 - \frac{P}{P_{adh}}}}{2} \right)^{\frac{4}{3}} - \frac{2}{3} \frac{a_0^2}{R} \left(\frac{1 + \sqrt{1 - \frac{P}{P_{adh}}}}{2} \right)^{\frac{1}{3}} \tag{5.3}$$

which gives $x_{contact}$ (the displacement at which the probe first contacts the surface), a_0 (the radius of the contact area at x_0 (Ebenstein, 2011)), and P_{adh}. Fitting the range of data from P_{adh} to point on the unloading curve where the force was equal to the magnitude of P_{adh} produced the most robust fit and an elastic modulus value closest to the baseline value from the detergent measurement. The reduced modulus is then calculated using

$$E_r = \frac{-3RP_{adh}}{a_0^3}$$

The modulus of the hydrogel was then calculated from the reduced elastic modulus (Ebenstein, 2011).

For the nanoindentation measurements, the detergent measurements gave baseline values of 2.22 ± 0.13 MPa for the reduced modulus of the sample with the smaller ratio of base to cross-linker and 0.50 ± 0.02 MPa for the reduced modulus of the sample with the larger ratio. Assuming Poisson's ratio has a value of 0.5, the elastic moduli of the two samples are 1.67 MPa and 0.38 MPa, respectively.

The first figure below compares the reduced modulus calculated with the various methods for the sample with a smaller base to crosslinker ratio, and the asterisks highlight the Young's modulus values that differ significantly from the baseline detergent measurement. The second figure is a similar comparison for the sample with a larger base to crosslinker ratio.

Figure 5.2. 2: The Young's moduli of the more crosslinked sample for different experimental
conditions calculated using various mechanical models, where the asterisks indicate
significantly differ from the baseline value (Ebenstein, 2011).
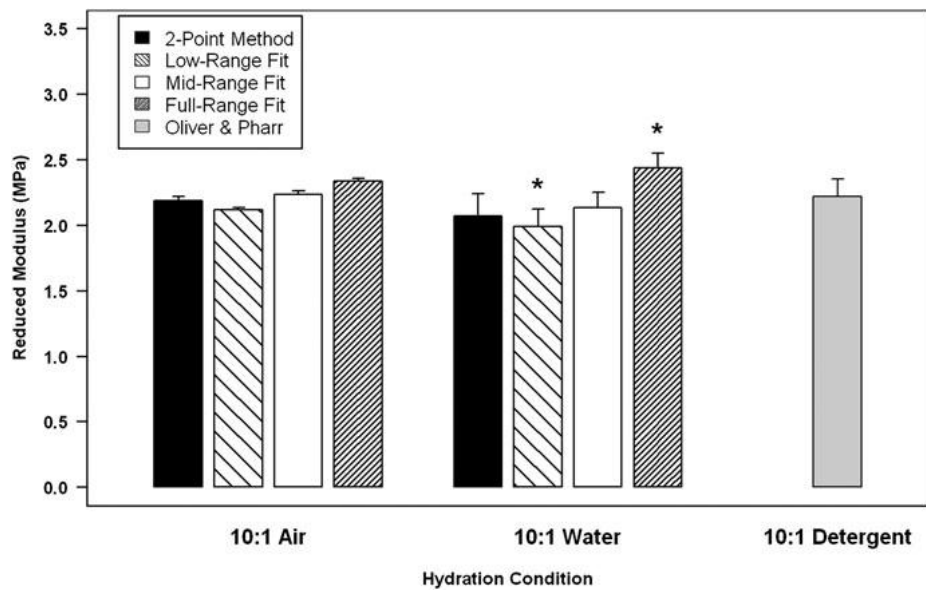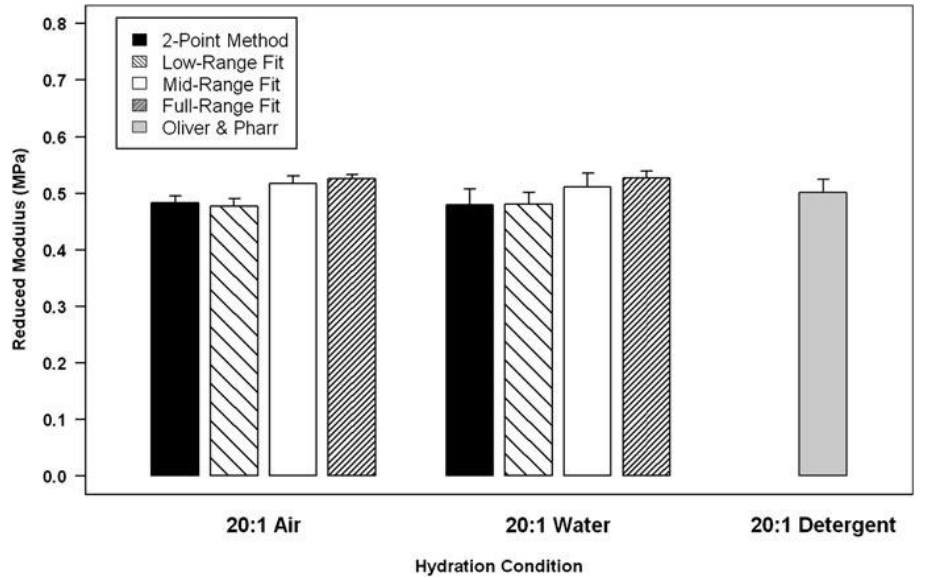

Figure 5.2. 3: The Young's moduli of the less crosslinked sample for different experimental
conditions calculated using various mechanical models (Ebenstein, 2011).

In contrast to the nanoindentation measurements, the quasi-static

indentation measurements in air and water resulted in a larger value of the

Young's modulus than the baseline measurements in detergent. Both the two-

point method and the curve fitting method employing the JKR model produced

values which did not differ dramatically in both water and air because they

accounted for adhesion and the effects of capillary forces between the tip and

fluid (Ebenstein, 2011).

This paper does not investigate viscoelastic effects and notes that the

moduli measured are the moduli when viscoelastic effects are negligible. In fact,

this method will be inaccurate if the time needed for the polymers to relax is

longer than the total possible indentation time. In such cases, a comprehensive

study of viscoelasticity within the JKR model may be necessary (Ebenstein,

2011).

5.3 M.J.N. JUNK, R. BERGER, AND U. JONAS. **26,** *LANGMUIR,* 7262-7269,

2010.

PNIPAm is famously temperature-responsive. The homopolymer has

potential applications in controlled drug delivery devices (see Chapter 3.2.2)

because the polymer and solvent phase separate close to the normal human body

temperature. When the phase separation occurs, the hydrogel shrinks as solvent is

expelled from the network. If a drug is contained in the fluid, this phase

separation will carry both the fluid and the drug into the environment, thereby

delivering the drug. The temperature at which this phase separation occurs is

known as the lower critical solution temperature (LCST). To design effective

controlled drug delivery devices – among other applications – the relationship

between temperature and mechanical properties must be known (Junk *et al.,* 2010).

Junk *et al.* determined that relationship between the mechanical properties of photo-crosslinked PNIPAm terpolymer (three monomer) films and the environmental temperature. The films were spin-coated onto silanized glass substrates and photo-crosslinked with UV light. When dry, the films were approximately 450 nm thick and swelled to a few microns thick. The sample was immersed in water in a fluid cell with a temperature-controlled scanner. Some of the probes used in the experiments were silanized so that the tip surface was hydrophilic, and the rest were plasma-cleaned so that the tip surface was hydrophobic. The measurements were made at a velocity of 5.4 μm/s (Junk *et al.,* 2010).

The temperature was increased and subsequently decreased from 293.15 K to 323.15 K in increments of 1, 2, or 5 K. Measurements were taken one minute after the temperature increase, at which time no thermal drift in the cantilever deflection was observed. The force curves for the increasing and decreasing temperature measurements were then compared. In all the measurements, the apparent indentation – the indentation relative to the maximum indentation measured at 50ºC – was measured. As a result, the goal was to compress each sample until the compression was approximately that measured at 50ºC (Junk *et al.,* 2010).

At 20ºC (293.15 K), the hydrogel is fully swollen. As expected, the

deformation of the hydrogel is large and reversible. Moreover, a large adhesive force between the tip and the film is observed. As the temperature was increased from 30ºC to 34 ºC, the slope of the extension curves increased significantly as the indentation and adhesive force both decreased significantly. At 34ºC, the hysteresis between the extension and retraction curves becomes much more pronounced than before, and the extension curve becomes linear. Moreover, the adhesive force and maximum indentation depth decrease significantly. All of these characteristics indicate that the hydrogel is hardening substantially with increasing temperature. At 40ºC, the hydrogel is stiffening, and a corresponding decrease in maximum indentation and adhesive force is observed. At 50ºC, the hydrogel has completely collapsed, and the extension curve has a nearly infinite slope. These curves serve as the hard reference state. The adhesion force increases slightly compared to measurements at slightly lower temperatures (Junk *et al.*, 2010).

These trends can be explained in terms of the volume transitions. When the hydrogel is fully swollen, the flexible network allows large, elastic deformations with large adhesive forces. But as the hydrogel phase separates, the water leaves the network, and the hydrogel becomes a relatively hard film of polymer molecules. Consequently, this film cannot be indented extensively. Junk *et al.* found that the volume collapse curve (graph of the apparent indentation versus the temperature) for each crosslink density is approximately sigmoidal (Junk *et al.,* 2010).

The Young's modulus was calculated using the Hertz model formulated for a conical indenter probing a planar surface. Although most nanoindentation measurements of Young's modulus employ a tip with a spherical bead, a sharp tip was used in these measurements because probing thickness changes requires a sharp tip. The Young's modulus was found to be exponentially related to the polymer volume fraction and inversely proportional to the swelling ratios, but no potential physical explanation was offered (Junk *et al.*, 2010).

Notably, the adhesion force was greatest at the point on the force curve where the apparent indentation (and, consequently, the actual indentation) was 0 nm. This result suggests that while the tip is withdrawing, the hydrogel adheres to the tip and, consequently, is drawn upward beyond the original surface height of the gel. Below the critical temperature (the temperature at which the hydrogel completely collapses), the adhesive force between the hydrophilic tip and the hydrogel below the critical temperature varies only slightly with temperature. But for temperatures close to the critical temperature, the adhesive force is significantly reduced from its value at lower temperatures. As the hydrogel deswells, the indentation and, therefore, contact area are significantly decreased, leading to a corresponding reduction in adhesive force. This hypothesis is supported by fitting the adhesive force versus temperature curve with a sigmoidal function, which has an inflection point with approximately the value of the critical temperature. Above this range around the critical temperature, the adhesive force undergoes small increases as the temperature is raised.

A comparable trend in the variations of the adhesive force around the critical temperature is observed between the hydrophobic tip and the hydrogel. When the temperature is both above and below the critical temperature – unlike the measurements with the hydrophilic tip – the adhesive force between the hydrophobic tip and the hydrogel is directly and strongly proportional to the temperature, and the slopes in both temperature regions are comparable. Greater uncertainty exists for measurements around the critical temperature for the hydrophobic tip than for the hydrophilic tip because around the critical temperature, the phase separation of the hydrogel and solvent is unstable, resulting in both hydrophobic and hydrophilic regions throughout the gel. The hydrophobic tip is more sensitive to these different regions, resulting in greater uncertainty. These regions can actually be imaged with the AFM, as shown in Figure 5.3.1 (Junk *et al.,* 2010):
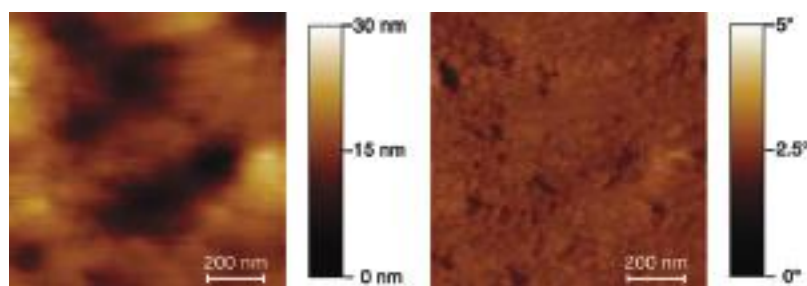
Figure 5.3.1: AFM image of hydrogel at 313.15 K (collapsed state) taken in tapping mode with hydrophilic tip. On the left is the topography image; on the right is the phase image.

This research helps us to understand the potential effects of temperature on the measured mechanical properties. Moreover, it emphasizes the importance of monitoring the temperature and accounting for those effects, especially around the critical temperature.

5.4. S. CAI, Y. HU, X. ZHAO, AND Z. SUO. **108,** *J. APPL. PHYS.,* 113514,

2010. AND Y. HU, E.P. CHAN, **110,** *J. APPL. PHYS.,* 066103, 2011.

The Suo group – (Cai *et al.*, 2010) and (Hu *et al.*, 2011) – used a curve-fitting technique and the poroelastic response of the hydrogels measured through nanoindentation to extract the shear modulus of the hydrogels. Cai *et al.* compared mechanical characteristics determined from compression with those from indentation, compared all experimental results to theory, and described the theoretical prediction of stress fields that are present only on short time scales. After the hydrogel samples were crosslinked and swelled completely, compressive force was applied suddenly with either a conical indenter or a compression plate. The indentation is then held constant. The force on the indenter or plate initially increases dramatically when the stress is applied and subsequently decreases as the indentation is held constant. This decrease is a result of the movement of the fluid in the gel. Eventually, the rate of this change in force decreases as the gel reaches a new equilibrium. The shear modulus and Poisson's ratio of the gel, as well as the "permeability of the solvent through the network," are then extracted from the relaxation curve (Cai *et al.*, 2010).

Biot's theory of poroelasticity is first formulated so that it can be applied to extract mechanical characteristics from relaxation curves obtained from compression tests. The short-time limit (instantaneously after compression) and long-time limit (a long time after the gel is first compressed) behaviors are

calculated using the resulting equations for stress and strain in the gel. The analysis reveals that the Poisson's ratio ν predicts the behavior of the gel. When a compressed gel reaches a new equilibrium with the surrounding solvent, none of the original solvent leaves the gel if $\nu \rightarrow \frac{1}{2}$. But some solvent does leave the gel if $-1 < \nu < \frac{1}{2}$ (Cai *et al.*, 2010).

Solving for the stress and strain fields in the gel, the authors obtain expressions for the displacement fields and plot these expressions to understand the behavior of the gel at various periods. The axial stress function is integrated over the surface area of the sample to produce the axial force equation *F(t)*. Plotting this equation generates a theoretical relaxation curve as a function of time, the shear modulus of the gel *G*, the contact radius *a*, and the diffusivity *D* in the form of

$$\frac{F(t) - F(0)}{F(0) - F(\infty)} = f\left(\nu, \frac{Dt}{a^2}\right) \tag{5.4}$$

where *F(0)* is the short-time limit of *F(t)* and *F(∞)* is the long-time limit of *F(t)*. The left hand side of the equation indicates how close the gel is to reaching an equilibrium state (Cai *et al.*, 2010).

The poroelasticity of the gel gives rise to a relaxation curve in which the force instantly peaks and then exponentially decreases as time passes. By normalizing the force with the area of the disk under investigation (nominal stress) and the time by the square of the radius, the relaxation curves for samples of various sizes are identical. The relaxation time of the hydrogel directly depends on the square of the radius of the sample. By comparing this

experimental curves with the theoretical relaxation curve obtained from the equation above with $F(t)$, one can obtain G, ν, and D. The values that the authors obtain are as follows: G=34.2 kPa; $\nu = 0.23$; and D=6.2*10^{-9} m^2/s, which are in excellent agreement with the values calculated from compression measurements (Cai *et al,* 2010).

Hu *et al.* also use poroelastic indentation to characterize gels but develop a particular mechanical characterization technique termed poroelastic relaxation indentation (PRI). PRI is a method of indentation in which the force relaxation curve is fit with the solution to the poroelastic boundary-value problem and correlates the poroelastic properties with the molecular characteristics (Hu *et al.*, 2011). Moreover, the solution to the poroelastic boundary-value problem is relatively simple, and, thus, the poroelastic constants can be calculated from the pororelastic relaxation curve with relative ease. The material constants determined using this method for indentation with conical and spherical indenters have been shown in previous research to be in good agreement with compression tests. But all previous research has assumed that the radius of contact of the indenter with the gel was much smaller than the thickness and surface area of the gels. Thin films of gels, where the thickness of the gel is the same order of magnitude as the contact radius, are used in many different applications, and this paper demonstrates that PRI can be used as a characterization method for thin gels.

In PRI, a gel of thickness d is indented by a spherical indenter of radius R

to a depth h, resulting in a contact radius a. Then the force is kept constant, and

the response force that the gel exerts on the indenter is recorded as a function of

time to produce a force relaxation curve. According to analysis of Yu *et al.*

(2010), whose work is cited in this paper, for a rigid, frictionless substrate

supporting the gel and indenter, the contact radius a is of the form

$$a = \sqrt{Rh} * l\left(\frac{\sqrt{Rh}}{d}\right) \tag{5.5}$$

The force $F(t)$ on the indenter has the form

$$F = \frac{8Gh\sqrt{Rh}}{3} * f\left(\frac{\sqrt{Rh}}{d}\right) \tag{5.6}$$

Neither $l(x)$ nor $f(x)$ depends on Poisson's ratio. As a becomes much smaller than

d, the contact area approaches that given by the Hertz model. In contrast, as a

becomes much larger than d, the contact radius approaches that of "a spherical

cap of height h" (Hu *et al.*, 2011). First, they determined the limit of $F(t)$

instantaneously after the gel is indented and secondly the limit of $F(t)$ after the gel

is indented for a long time period. They solve the poroelastic problem to obtain a

dimensionless function which does not depend on Poisson's ratio. Numerical

analysis of this function shows that when all the other variables are held constant,

the relaxation time decreases as the thickness of the gel decreases (Hu *et al.*,

2011).

This function is then solved to obtain a dimensionless function that is

equal to the normalized force. This function can then be fit to the indentation-

time curve where both indentation and time are normalized. The average value of

the storage modulus extracted was 740 ± 30 kPa, of Poisson's ratio 0.34 ± 0.03, and the diffusivity constant $(3.1 \pm 0.2)*10^{-9}$ m^2/s. These values agree with previously reported values (Hu *et al.*, 2011).

   This paper emphasizes the considerable effect of poroelasticity on the mechanical properties of hydrogel thin films. Thus, in this thesis research, we probed a range of rates at which force is applied to begin to probe the time-dependent behavior. Moreover, we sought here to examine the time-dependent behavior in terms of the JKR model, which the research by the Suo group did not.

6. EXPERIMENTAL METHODS

SUMMARY

In this chapter, I will summarize the experimental system and characterization procedure used in these experiments. First, I will discuss the materials and cite a paper in which the interested readers can read the details of the synthesis process. Second, I will describe the actual samples on which I took measurements. Third, I will briefly summarize the measurement setup and procedure. Finally, I will discuss the procedure used to calculate the material properties from the experimental data collected.

6.1. MATERIALS

We investigated thin films of poly(*N*-isopropylacrilamide-co-benzephenone-co-acrylic acid-co-rhodamine B methacrylate). Specifically, the films were 87.3 mol % *N*-isopropylacrylamide, 7.0 mol % benzephenone, 5.5 mol % acrylic acid, and 0.2 mol % rhodamine B-labeled methacrylate. Interested readers should read the paper by Kim *et al.* (2012) published in *Soft Matter* to learn more about the synthesis of the polymer.

The measurements were taken in a neutral buffer solution (pH = 7.4). Two neutral solutions of different ion concentration were used for the different experiments. The solutions were prepared either from powder purchased from

Sigma Aldrich or from a standard recipe. The powder purchased from Sigma

Aldrich was mixed with deionized water so that the resulting solution was 0.318

M NaCl and 0.0027 M KCl. The second solution was prepared by dissolving 0.05

g of sodium phophate monobasic monohydrate ($NaH_2PO_4 - H_2O$), 0.17 g sodium

phophate dibasic heptahydrate ($Na_2HPO_4 - 7H_2O$), and 0.058 g NaCl in 10 mL

deionized water and then diluting the solution 100 times. The resulting solution

was 1 mM NaCl.

6.2 SAMPLE PREPARATION

Chips of silicon wafer were silanized, and poly(HEMA-co-BP) (2 wt%,

approximately 31.2 mg/mL) Pyridine solution was spin-coated at 2000 rpm

for 60 seconds onto the silicon wafer chip to improve adhesion between the

hydrogel and the substrate. PNIPAm-co-BPAm-co-AAc-RhBMA was dissolved

in Chloroform to form 1 wt% (approximately 15.6 mg/mL) solution. A 50-100

µL drop of copolymer solution in chloroform was spread onto the poly(HEMA-

co-BP), and the solvent was slowly evaporated over 7 to 9 hours at 45ºC in a

closed glass container (0.13 oz capacity glass jar, Freund Container). To

crosslink the sample, the film was exposed to ultraviolet light through the 10X

objective of a fluorescence microscope (365 nm, 38.7 mW/cm^2 for the first

template of samples – see below – and 6.2 mW/cm^2 for the second template of

samples) through a series of photomasks to control the exposure time

(corresponding to the irradiation dosage) and the dimensions of exposed regions

on the hydrogel film. Any un-crosslinked polymer was then washed away using an water-ethanol mixture (1:2 by volume). The dry thickness of the films was then measured using a stylus profilometer (Dektak, Veeco).

Two different templates of samples were prepared. The first series, shown in Figure 6.2.1, had regions of two different crosslinking densities. The features (squares, circles, or rectangles) were exposed for shorter lengths of time than the surrounding matrix. As a result, the features were less crosslinked than the surrounding matrix. The features thus swelled more than the matrix when the film was induced to swell. The dimensions of the samples are also depicted in Figure 6.2.1.

Squares : 150×150 μm^2
Interspacing : 100 μm
Matrix : 1350×1350 μm^2

Circle : 150 μm diameter
Interspacing : 100 μm
Matrix : 1350×1350 μm^2

Rectangles : 100×150 μm^2
Interspacing : 150 μm
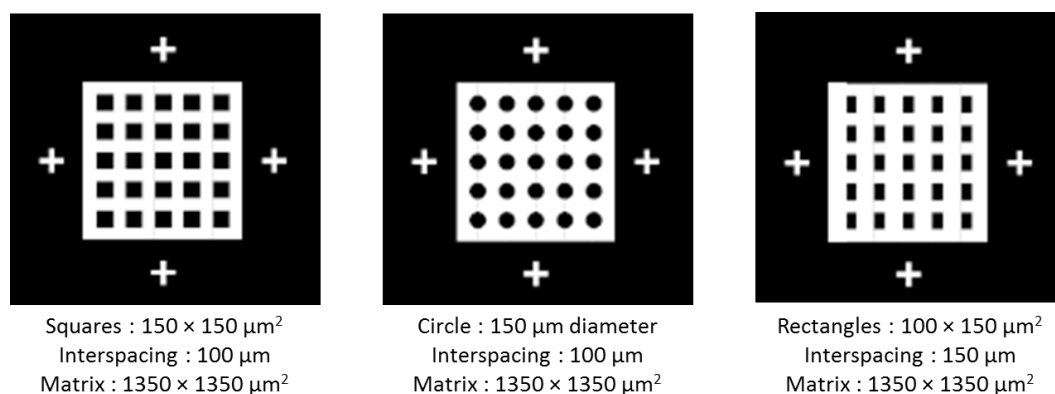Matrix : 1350×1350 μm^2

Figure 6.2. 1: First sample template and dimensions

The second type of sample was a strip of hydrogel with 7 different rectangles, each of which had a different exposure time and, thus, different crosslink density, as shown in Figure 6.2.2.

(a)

No matrix
Rectangles : $100 \times 200 \ \mu m^2$

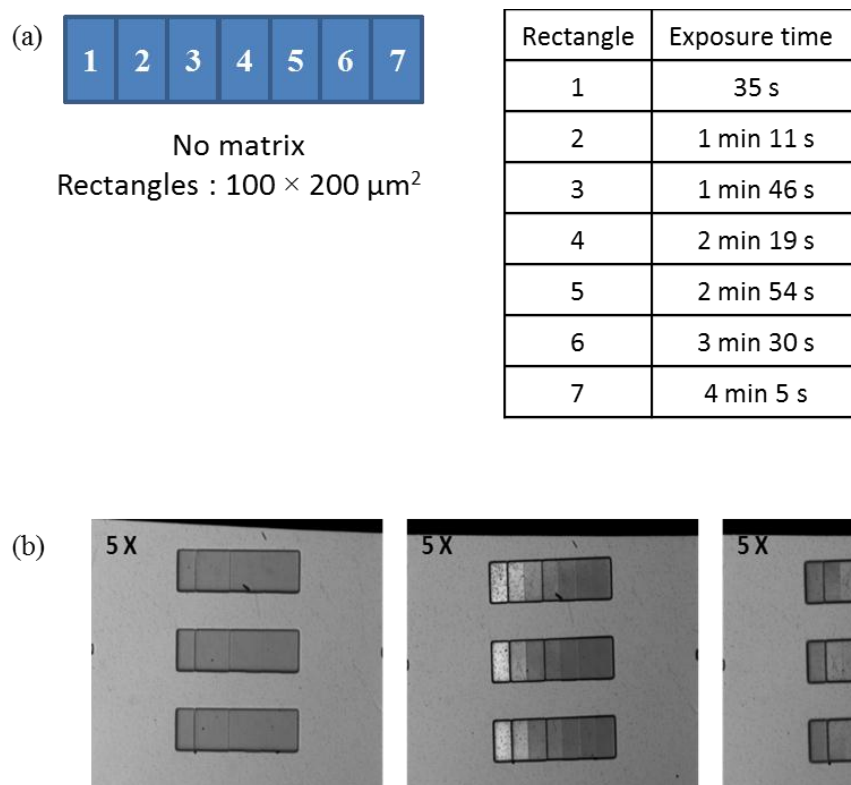| Rectangle	Exposure time
1	35 s
2	1 min 11 s
3	1 min 46 s
4	2 min 19 s
5	2 min 54 s
6	3 min 30 s
7	4 min 5 s

(b)

Figure 6.2. 2: (a) second sample template and table of crosslinking times; (b) image of film during development

These samples were fabricated at the University of Massachusetts Amherst by Dr. MyungHwan Byun. These samples were then transported to Mount Holyoke College. Once at Mount Holyoke College, these silicon chips were glued onto a larger substrate, either a glass microscopic slide which had been wiped with isopropynol or a magnetic puck which had also been wiped with isopropynol. A two-part epoxy was used, and the epoxy was allowed to cure for at least 15 minutes before any further steps were taken.

Before measurements, the samples were stored dry in petri dishes of which

the top had been wrapped in tin foil to reduce any additional crosslinking by

ambient light. Initially, the bottom half of the Petri dish was also wrapped in tin

foil, but this procedure was abandoned when I observed that wrapping only the

top helped to decrease evaporation of the PBS and to encourage sample hydration.

At least 1 hour before measurements, the samples were completely immersed in a

neutral buffer (pH = 7.4) solution so that the hydrogel had achieved swelling

equilibrium before any measurements began.

6.3 AFM INDENTATION MEASUREMENTS

Atomic force microscopy (AFM) is used in a variety of applications and is

well-adapted to perform micro- or nanoindentation experiments. Every AFM has

three major components – an AFM stage, control electronics, and a computer. In

the Asylum AFM that I was using in my experiments, the AFM stage consists of

the AFM head, a sample holder, and a platform which isolates the samples and

reduces noise from mechanical vibrations. The AFM head includes the scanner

which moves the AFM probe, the force sensor (to help control the movement of

the tip), and an optical microscope to view samples (Eaton *et al.*, 9). The control

electronics move the probe in all three directions of a rectangular Cartesian

coordinate system (i.e., in the x-, y-, and z-directions), oscillate the probe if

required in the experiment (Eaton *et al.*, 28), record data such as force and

deflection so that it can be read by the computer (Eaton *et al.*, 9), and relay this

data to the computer (Eaton *et al.*, 28). The software in the computer is used to set parameters for measurements and to acquire and display data collected with the AFM head (Eaton *et al.*, 9).

In the DSI measurements I was performing with the AFM, I use the AFM to measure the force exerted on the probe (also known as the tip) by the material in response to deformation produced by the probe. In the Asylum AFM, an optical lever system is used to sense and control the force. In an optical lever system, a beam of collimated light is bounced off of the back of a reflective cantilever and hits a photodiode divided into quadrants (Eaton *et al.*, 22). The "deflection" measures the vertical displacement of the laser spot on photodiode, and the "lateral" measures the horizontal displacement of the laser spot on the photodiodiode, all relative to the center of the photodiode (Eaton *et al.*, 23). When the tip's spring constant is determined using thermal motion, the deflection is correlated to the force exerted on the tip; therefore, deflection can now be converted into force on the tip during measurements (Eaton *et al.*, 42-44).

As the probe indents the sample, the probe is bent, changing the deflection. The indentation continues until the deflection reaches the trigger point (the force the user specified with the computer before the indentation began). The tip then begins to retract. Throughout this process, the displacement of the tip and corresponding force exerted on the probe are recoded, producing a force-distance curve (Eaton *et al.*, 35-36). Because the AFM measures the response of a material to indentation, we need mechanical models, which describe the response

of a material based on its material properties, to determine material properties from AFM measurements.

The tips used in these measurements were ordered from NanoAndMore and consisted of a diving-board cantilever at the end of which a silicon dioxide bead with a diameter of 3.5 μm was attached. The bead was needed to reduce the penetration depth and thereby minimize any substrate effects on the measured Young's moduli. The spring constant of the cantilever was reported to be 2.8 N/m but could range from 0.5 N/m to 9.5 N/m. These spring constants were slightly larger than but the same order of magnitude as the spring constants measured for the films.

To calibrate the tip, the tip was loaded into the AFM head and manually lowered to contact a glass slide that had been wiped previously with isopropyl alcohol. Two force curves were then taken. Using the slope of the second extension curve in the region where the tip was contacting the slide, the deflection was correlated with the voltage. Thermal motion of the tip was subsequently measured to determine the exact spring constant of each individual tip. Once the spring constant was determined, a drop of fluid was placed on the sample, and another drop of fluid was placed on the tip. The AFM head was then replaced, and the tip brought into contact with the sample. Again, two force curves were taken in fluid, and the slope of the second curve used to correlate the deflection with the voltage.

Two experimental setups were used in this thesis research. In the first, the

samples were glued to glass slides. Once the tips were calibrated, the sample was

loaded onto the AFM stage and secured with two magnets as shown in Figure
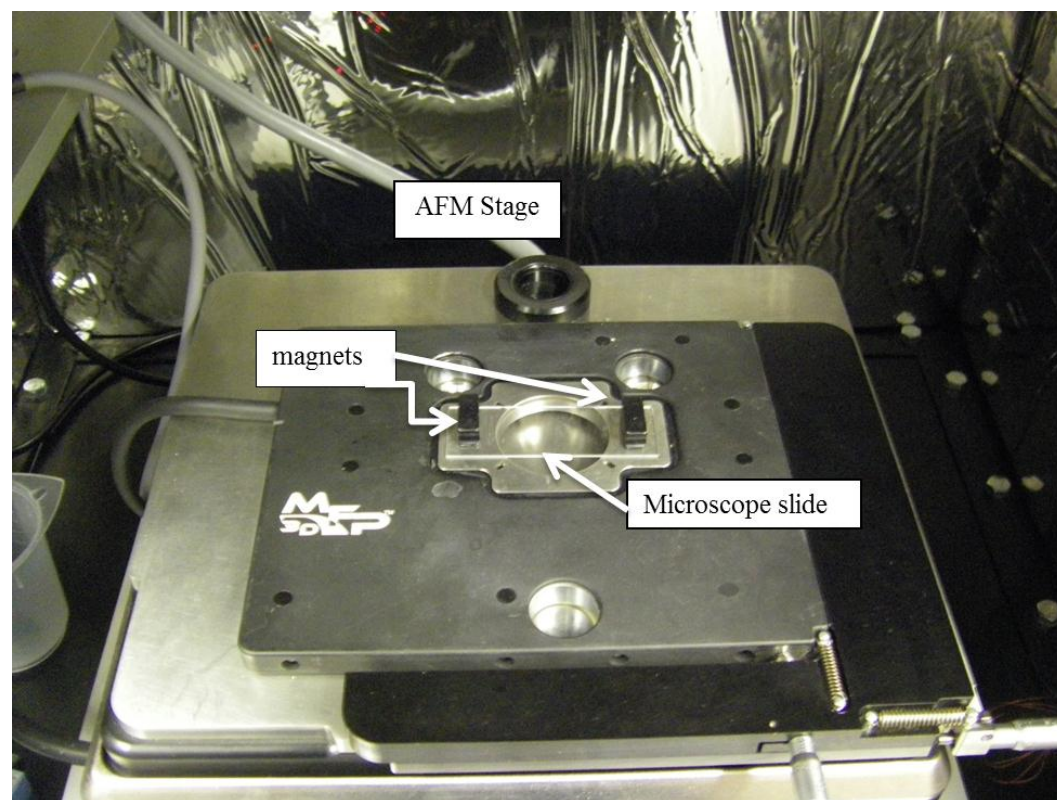
6.3.1.

Figure 6.3. 1: first experimental setup

In the second setup, the sample was glued to a magnetic puck. The sample

was then loaded into the polymer fluid cell and secured with another magnet on

the underside the sample dish of the fluid cell. In this setup, the temperature was

monitored and recorded throughout the experiment.

6.4 CALCULATION OF MATERIAL PROPERTIES

The mechanical properties of the hydrogels were calculated using the

Johnson-Kendall-Roberts mechanical model because this model accounts for the effects of the considerable adhesion in our measurements. In particular, the model was applied to the force curves using the "Two-Point Method" outlined by Ebenstein (2011). This analysis required that the force and displacement at two points on the retraction curve of the AFM force curve be extracted. As shown in Figure 6.4.1, the first point needed is the displacement (x_0) where the force on the AFM tip is first zero. The second point is the minimum of the extension curve, where the AFM applies just enough force to overcome the maximum adhesive force between the tip and sample (labeled x_{adh} and F_{adh} in the figure below); as a result, the magnitude of the force at that point is the magnitude of the maximum adhesive force between the tip and sample.
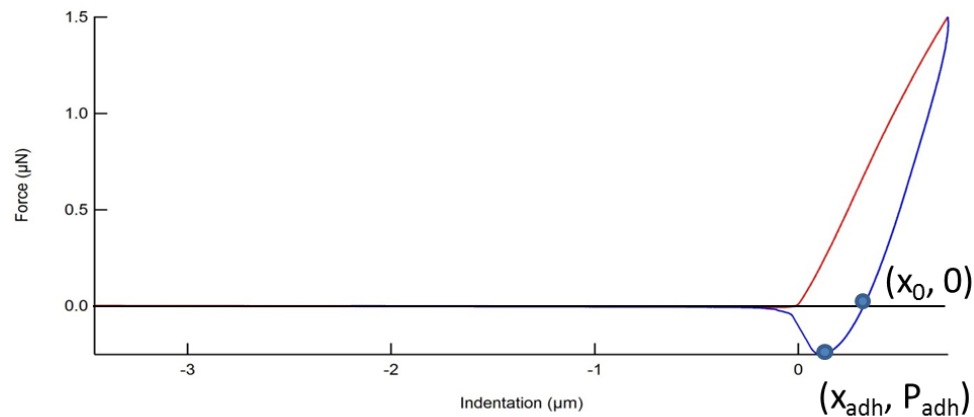

Figure: 6.4. 1: Representative force curve with the two points used in the two-point method labeled with blue markers

The displacements and forces at these two points are then used in the following equation:

$$E_r = \frac{-3P_{adh}}{\sqrt{R}} \left[\frac{3(x_0 - x_{adh})}{1 + 4^{-\frac{2}{3}}} \right]^{-\frac{3}{2}}$$

(6.1)

This equation gives the reduced modulus of the sample at that point. The reduced

Young's modulus is a combination of the Young's modulus of the sample and of

the tip:

$$\frac{1}{E_r} = \frac{1 - v_s^2}{E_s} - \frac{1 - v_t^2}{E_t}$$

(6.2)

When the Young's modulus of the sample is much smaller than that of the tip (E_s

is much smaller than E_t, as is the case where the sample is much softer than the

indenter), the second term can be neglected, and

$$E_s = (1 - v_s)E_r$$

(6.3)

(Ebenstein *et al.*, 2011).

The process was automated with code in Igor, the software used to analyze

data from AFM measurements. Simultaneously with calculation of the elastic

moduli of the hydrogels, the Tabor parameter was calculated.

7. RESULTS

SUMMARY

This chapter summarizes experimental results. Two different templates of samples were indented. Each region on the film in the first template, described in section 7.1, was exposed either for 3 minutes or for 1 minute, resulting in only two different crosslink densities on this sample. The second template, described in section 7.2, contained seven regions with successively increasing exposure time. The Young's moduli calculated from the force curves collected on each sample template are summarized in the respective sample, and the graphs of the Young's moduli versus velocity are presented. As expected, the Young's moduli for more crosslinked regions are larger than the values for the less crosslinked regions. In addition, as the speed at which force is applied increases, the measured moduli increase, revealing time dependent behavior.

7.1 SAMPLES WITH TWO DIFFERENT CROSSLINK DENSITIES

One type of samples probed had more crosslinked regions and less crosslinked regions. The more crosslinked region, the matrix, measured 1350 by 1350 μm^2 and contained 25 less-crosslinked regions (the features), which were squares, circles, or rectangles. Each square measured 150 by 150 μm^2, and each circle had a diameter of 150 μm. The rectangles measured 100 by 150 μm^2. At

least 100 μm were left between each feature. To achieve this difference in crosslinking, the matrix was exposed for a longer time than the features. In the case of the samples probed, the matrix was exposed for a total of 3 minutes. The matrix was first exposed for 2 minutes, with the light prevented from reaching the features. Then the entire film was exposed for 1 minute so that the features were crosslinked for a total of 1 minute.

AFM measurements were taken on each region. These force curves were analyzed using the two-point method outlined by Ebenstein (2011) and summarized in section 6.4, which extracts mechanical properties from force curves using the JKR theory. In this method, two points are extracted from every curve. These two points were then used to extract the reduced modulus of the material at that location on the film, and the reduced modulus was used to calculate the Tabor parameter, summarized in section 4.4.7. All the Tabor parameters were greater than 5, indicating that the Johnson-Kendall-Roberts (JKR) model was appropriate. The two-point method is a simple way to apply the JKR model and extract mechanical properties from force curves.

Because hydrogels are both viscoelastic and poroelastic, we expected the mechanical behavior of the hydrogels to depend on time, specifically on the rate at which the force was applied (the velocity). Consequently, we probed a range of velocities. Averaging the Young's moduli values at each velocity, we produce several plots, all with log scales on both axes. Figure 7.1.2 plots the average Young's modulus against the average velocity with plots for both the features and

matrix on the same graph. Figure 7.1.3 plots the Young's modulus measured on the less crosslinked features of the film against the velocities, and Figure 7.1.4 is the corresponding plot for the more crosslinked matrix. The error bars on all of the graphs are the standard error of the mean, which is a measure of how accurately the mean of the measurements describes the true mean.
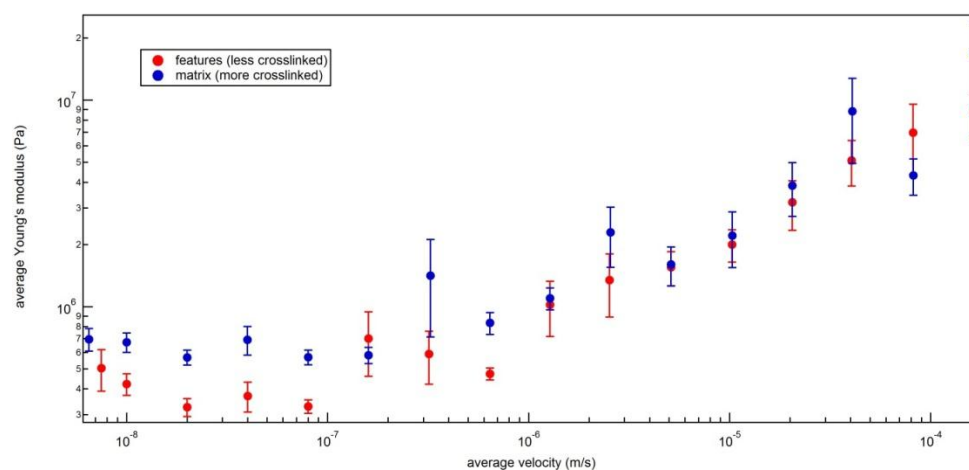

Figure 7.1. 1: The average Young's modulus for both the less crosslinked and more crosslinked regions plotted against the average velocity, where both axes use a log scale.
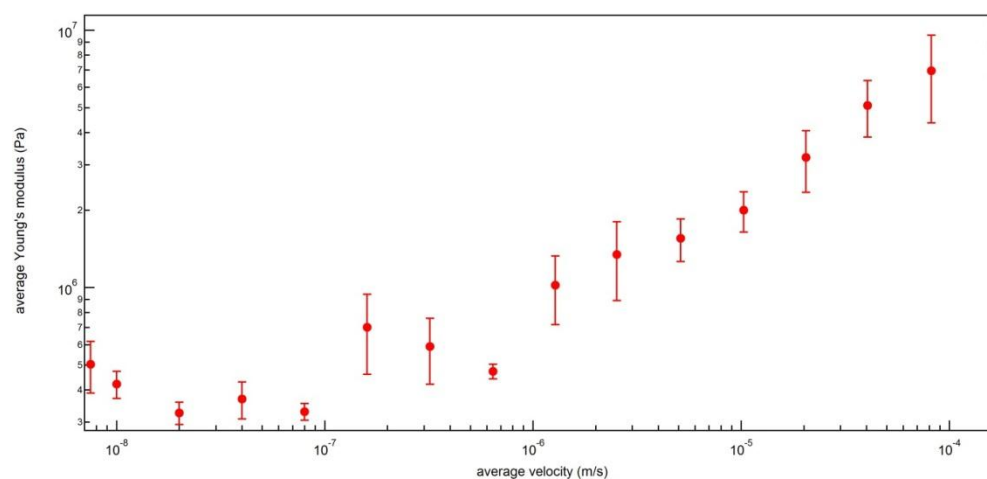

Figure 7.1. 2: The average Young's modulus for the less crosslinked regions plotted against the average velocity, where both axes use a log scale.
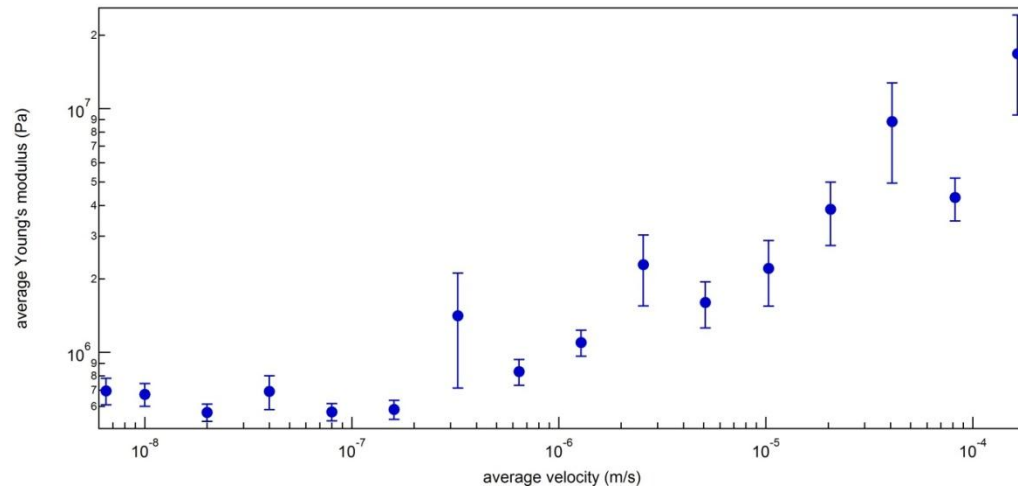
Figure 7.1. 3: The average Young's modulus plotted against the average velocity, where both axes use a log scale.

These graphs show that in the low-velocity region, the value of the Young's modulus is relatively constant. But as the velocity increases past approximately1.28 μm/s (the ninth point from the left), the Young's modulus for both the matrix and features increases dramatically by a little over an order of magnitude in both cases.

For a more intuitive understanding of the behavior of the Young's modulus, we plotted the Young's modulus with the difference between x_0 and x_{adh} (the two indentations extracted from each force curve and used in the two-point method) and with the maximum adhesive force measured, P_{adh}. Further analysis suggests that value of the difference between x_0 and x_{adh}, $(x_0 - x_{adh})$, in the two-point method has the greatest impact on the value of the modulus E, as indicated in the plots below. Figures 7.1.4 and 7.1.6 plot the average Young's modulus versus $(x_0 - x_{adh})$ at the corresponding velocity using a log scale on both axes. Figures 7.1.5 and 7.1.7 plot the average Young's modulus versus P_{adh}. Figures

7.1.4 and 7.1.5 show the dependence for the more crosslinked regions, and

Figures 7.1.6 and 7.1.7 show the dependence for the less crosslinked regions. We

see a clear relationship between Young's modulus and $(x_0 - x_{adh})$ as expected by

the relationship for the reduced modulus, while the values for P_{adh} are more
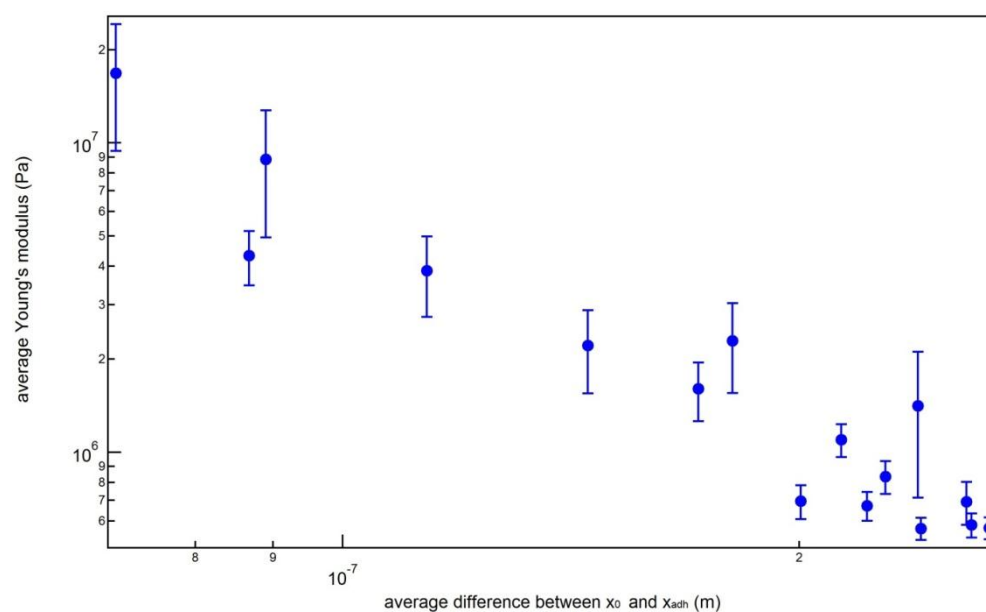
scattered.

Figure 7.1. 4: The average Young's modulus versus the average $(x_0 - x_{adh})$ for the more crosslinked region of the film.
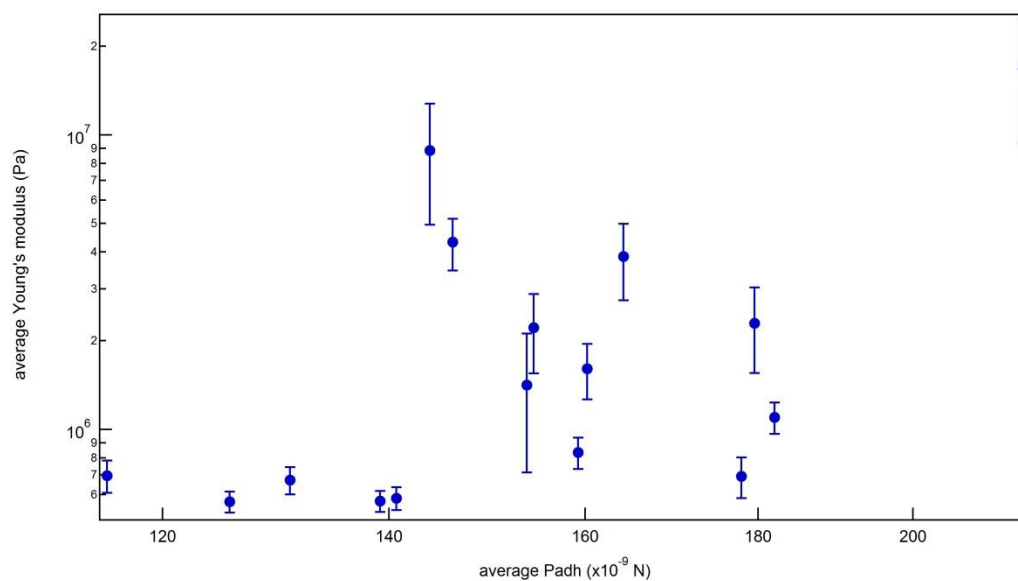
Figure 7.1. 5: The average Young's modulus versus the average maximum adhesive force P_{adh} for the more crosslinked region of the film.
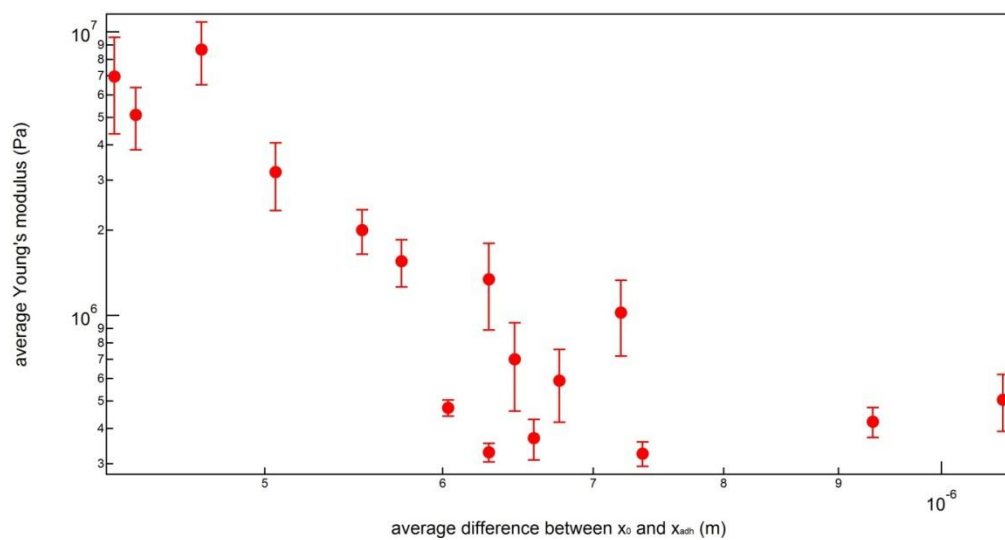

Figure 7.1. 6: The average Young's modulus versus the average ($x_0 - x_{adh}$) for the less crosslinked region of the film.
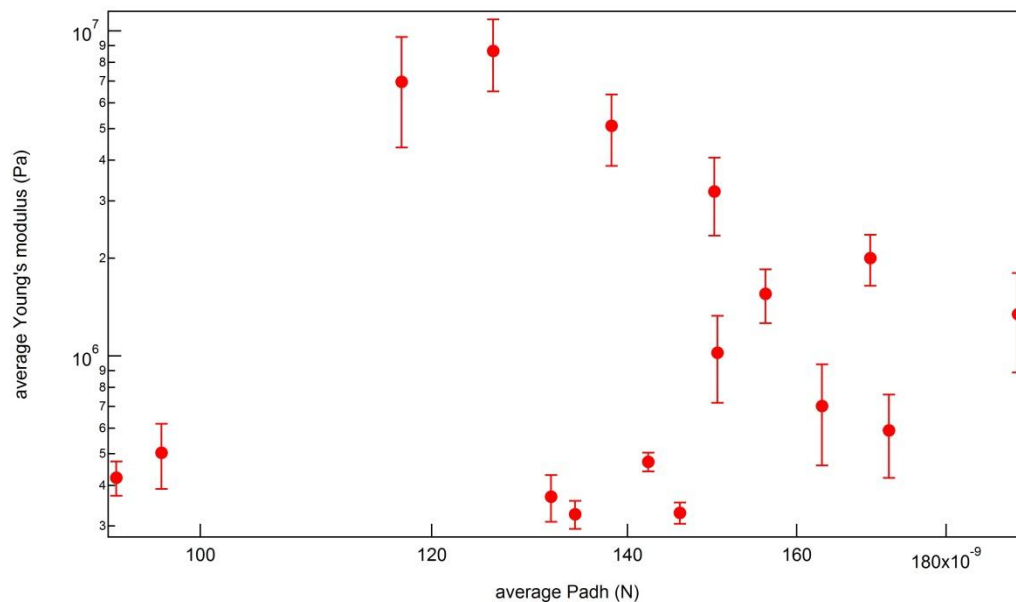
Figure 7.1. 7: The average Young's modulus versus the average maximum adhesive force P_{adh} for the less crosslinked region of the film.

These figures were used to gain a more intuitive feel for the two-point

method and an understanding of the dominant factor on the value of the Young's

modulus. As expected from examining the equation used in the two-point method

(see equation 6.1), comparing Figures 7.1.4 and 7.1.5 show that for the more

crosslinked regions, when $(x_0 - x_{adh})$ is small – in which case the modulus and

velocity are higher – P_{adh} is generally larger. The same trend is evident in the less

crosslinked regions, as evident in Figures 7.1.6 and 7.1.7. In Figure 7.1.1, the

Young's modulus is relatively constant in the low-velocity regime and uniformly

different between the more crosslinked regions (larger Young's modulus) and the

less crosslinked regions (smaller Young's modulus). But at high velocities, the

Young's moduli values appear to converge. Likewise, $(x_0 - x_{adh})$ is uniformly

different for the two crosslink densities across all velocities, indicating that the

value of P_{adh} probably becomes a considerable factor in determining the

convergence of the Young's moduli at high velocities.   The variability in the

value of *Padh* may explain the variability in our data.

7.2. SAMPLE WITH SEVEN DIFFERENT CROSSLINK DENSITIES

The other sample template on which measurements were taken consisted

of three long strips, each with 7 rectangles of increasing exposure time and

therefore increasing crosslink density, as shown in Figure 7.2.1. The film had a

dry thickness of about 5.2 μm.

(a)

| 1 | 2 | 3 | 4 | 5 | 6 | 7 |

No matrix
Rectangles : 100×200 μm^2

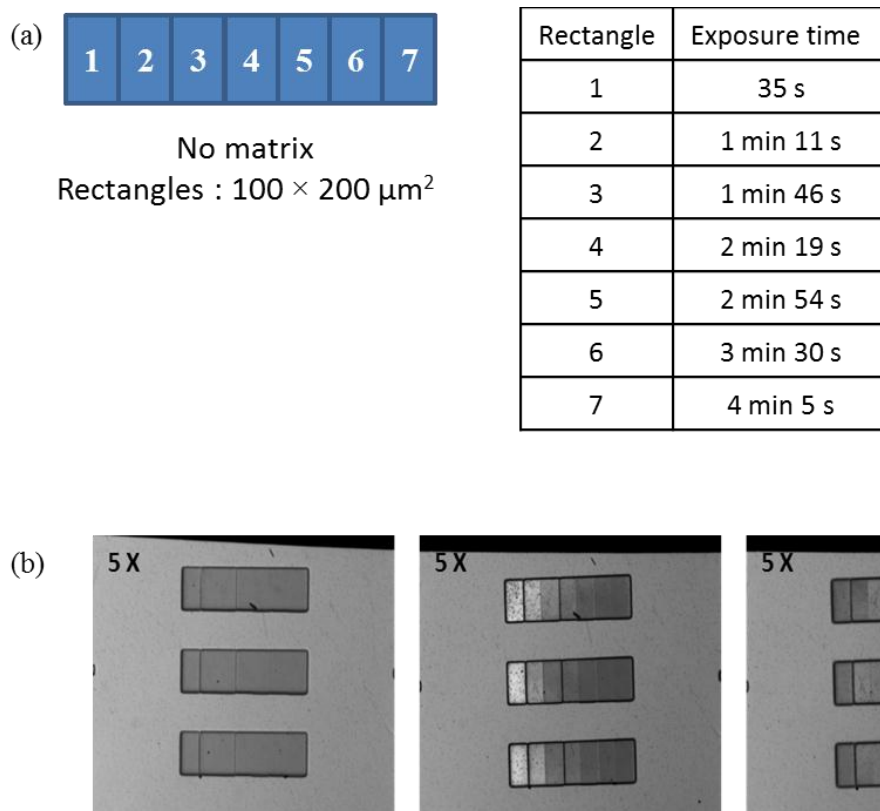| Rectangle	Exposure time
1	35 s
2	1 min 11 s
3	1 min 46 s
4	2 min 19 s
5	2 min 54 s
6	3 min 30 s
7	4 min 5 s

(b)

Figure: 7.2. 1: Sample specifications for range of different exposure times: (a) schematic drawing of the template of the sample; (b) image of the sample during development.

Although these data are only preliminary, we find that each rectangle shows the same trend as the two-crosslinked film: the Young's modulus increases with increased exposure time. Each of following figures plots the average Young's modulus against the average velocity for each rectangle, and the figures are in the order of increasing exposure time (and, therefore, crosslink density). Figure 7.2.9 displays all those points on one plot for easier comparison. In all figures, the error bars are the standard error of the mean.
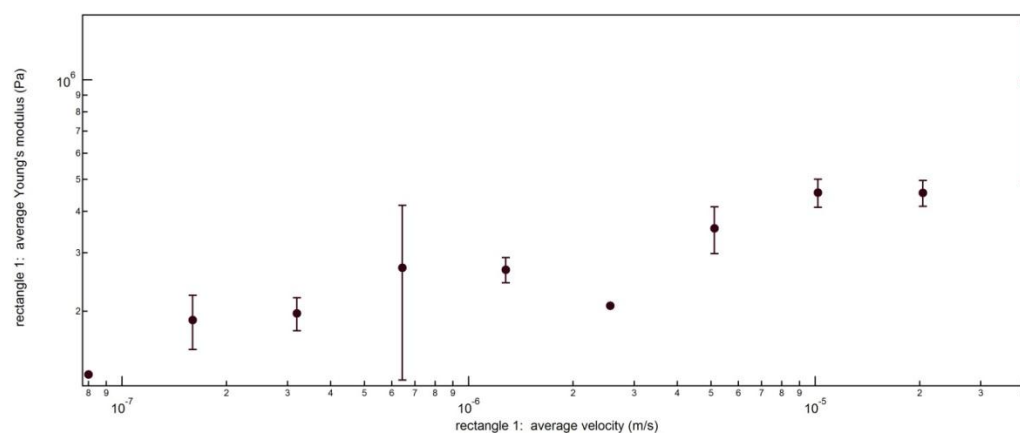

Figure: 7.2. 2: Average Young's modulus plotted again velocity for rectangle exposed for 35 s.
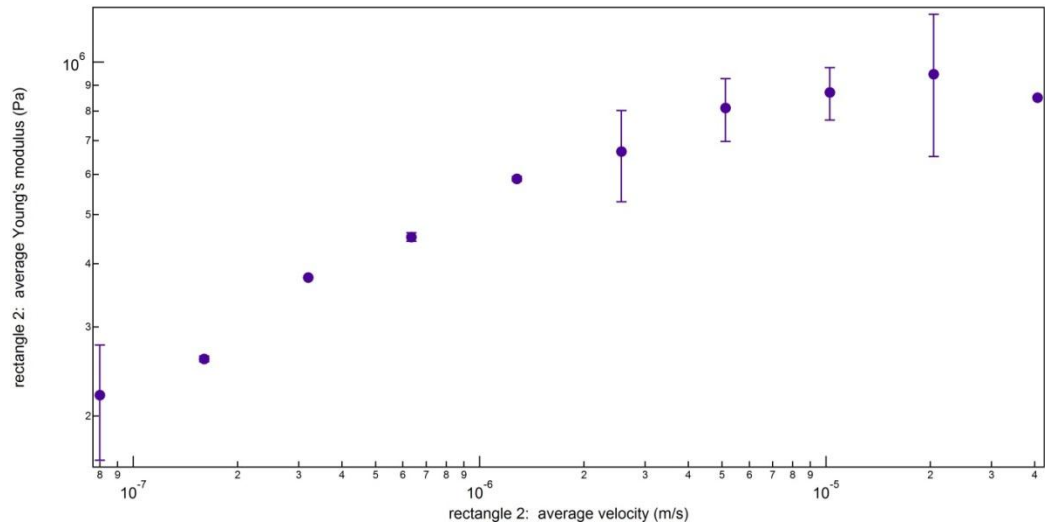
Figure: 7.2. 3: Average Young's modulus plotted again velocity for rectangle exposed for 1 min 11 s.

Figure: 7.2. 4: Average Young's modulus plotted again velocity for rectangle exposed for 1 min 46 s.

Figure: 7.2. 5: Average Young's modulus plotted again velocity for rectangle exposure for 2 min 19 s.
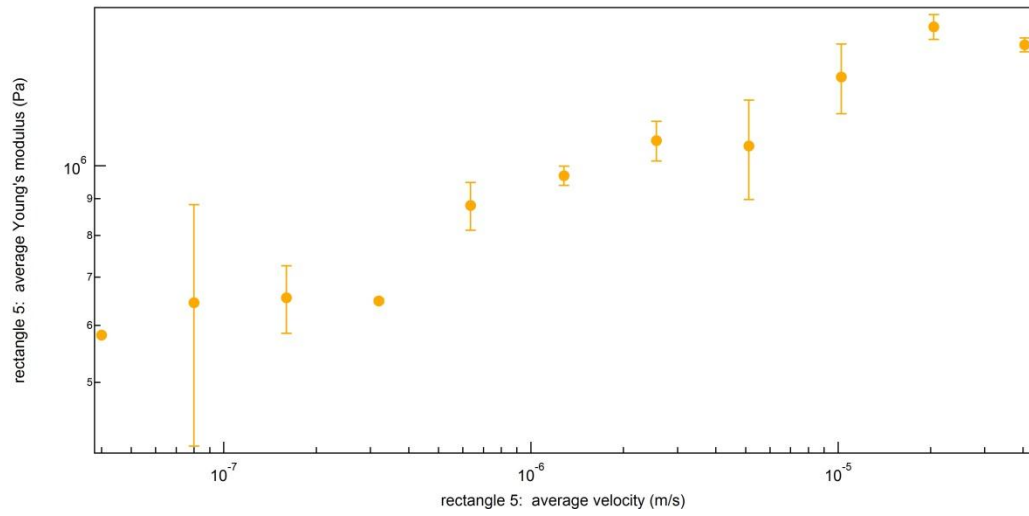
Figure: 7.2. 6: Average Young's modulus plotted again velocity for rectangle exposed for 2 min 54 s.
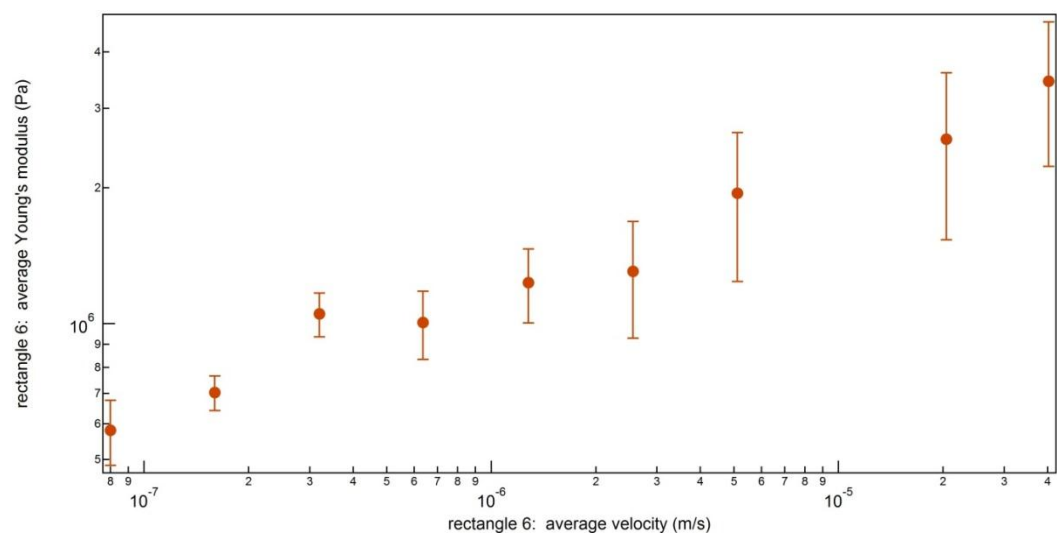
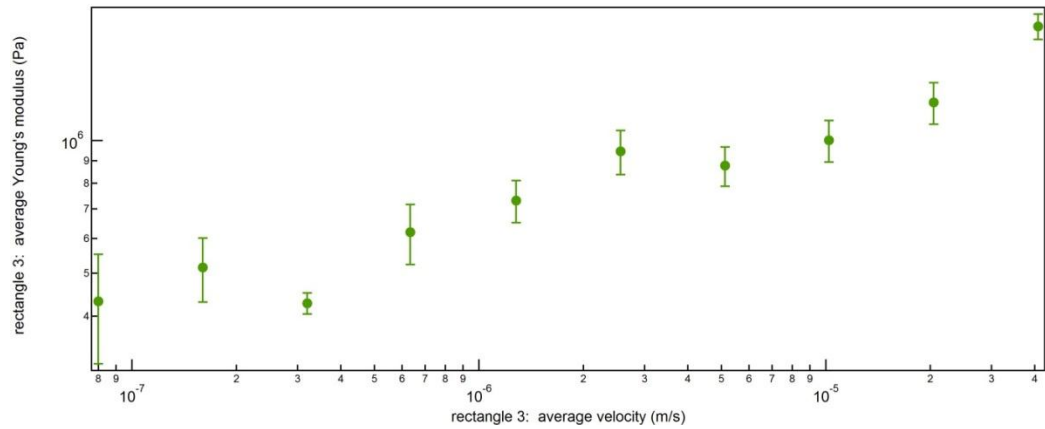Figure: 7.2. 7: Average Young's modulus plotted again velocity for rectangle exposed for 3 min 30 s.
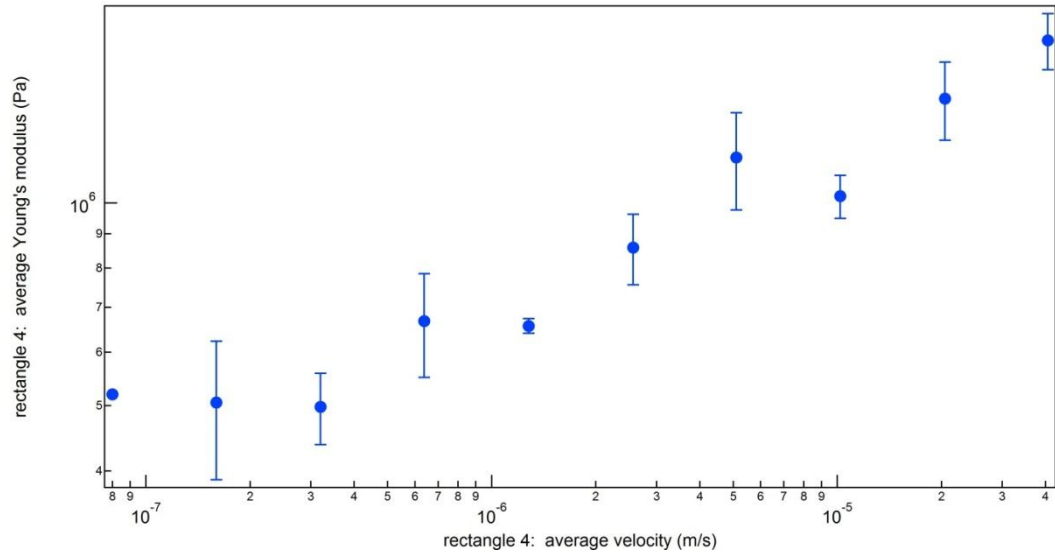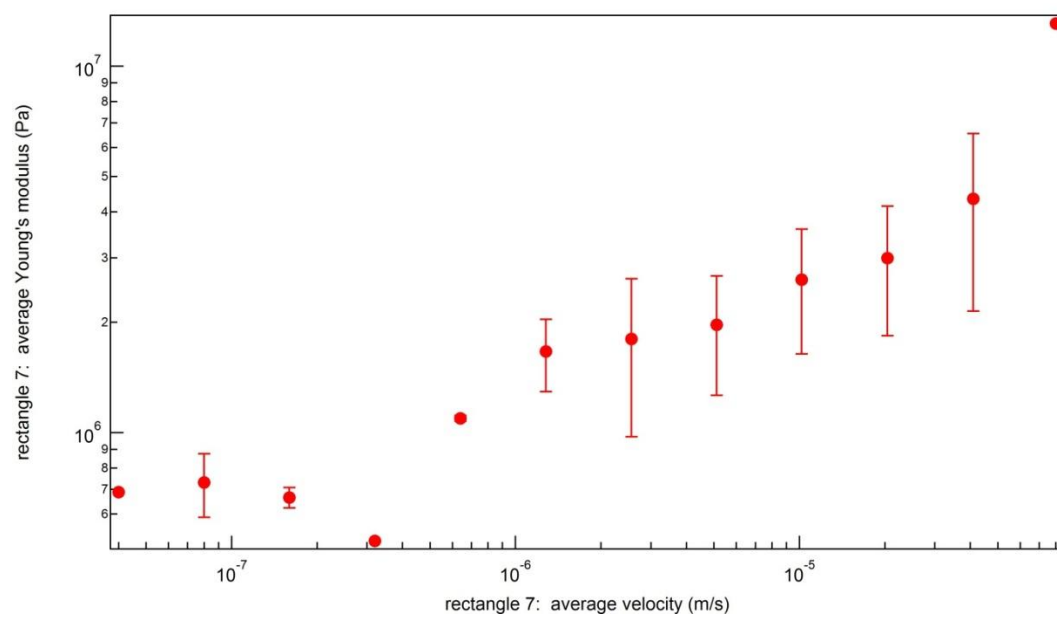

Figure: 7.2. 8: Average Young's modulus plotted again velocity for rectangle exposed for 4 min 5 s.
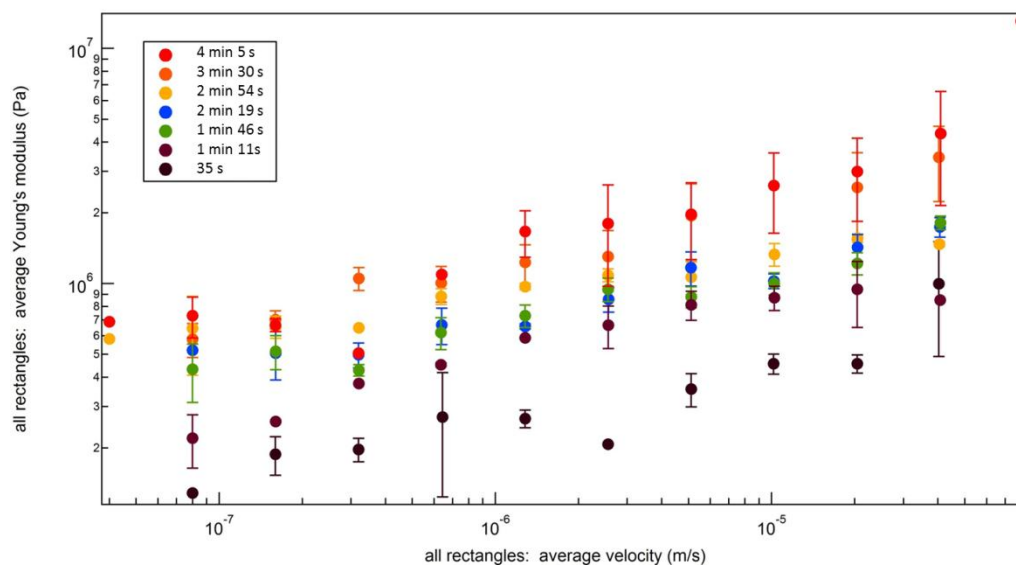
Figure: 7.2. 9: Average Young's modulus plotted again velocity for all the rectangles.

The force curves from this sample were analyzed using the two-point method

outlined by Ebenstein (2011) as outlined in section 7.1. If we examine the

Young's moduli measured at 80 nm/s for all the different crosslink densities, we

obtain Figure 7.2.10. Likewise, if we examine the Young's moduli measured at

1.28 μm/s for all the different crosslink densities, we obtain Figure 7.2.11.
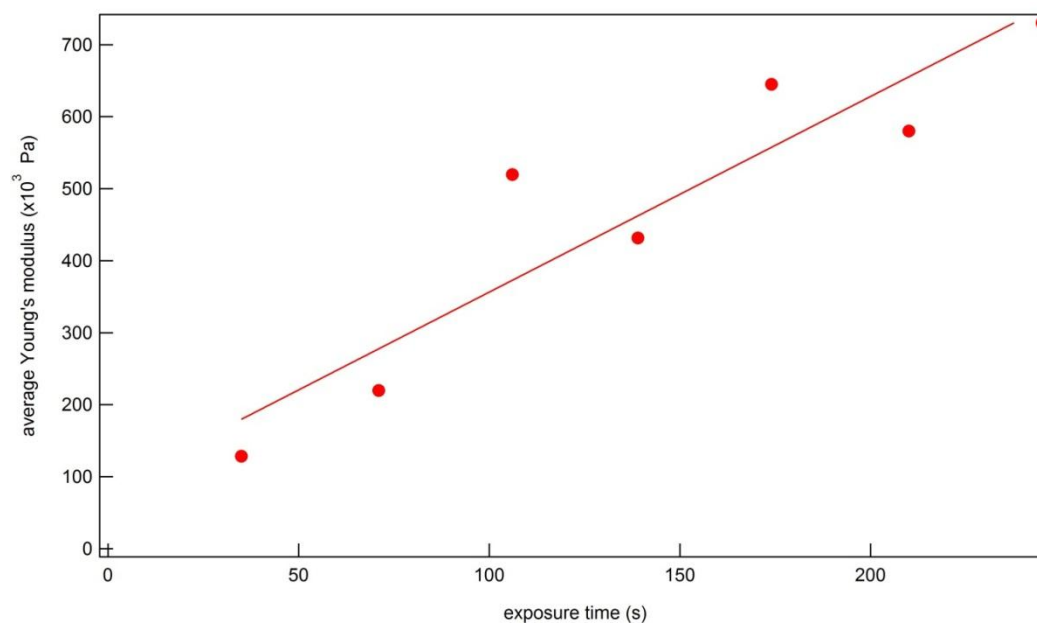
Figure: 7.2. 10: Young's modulus compared to exposure time for 80 nm/s.
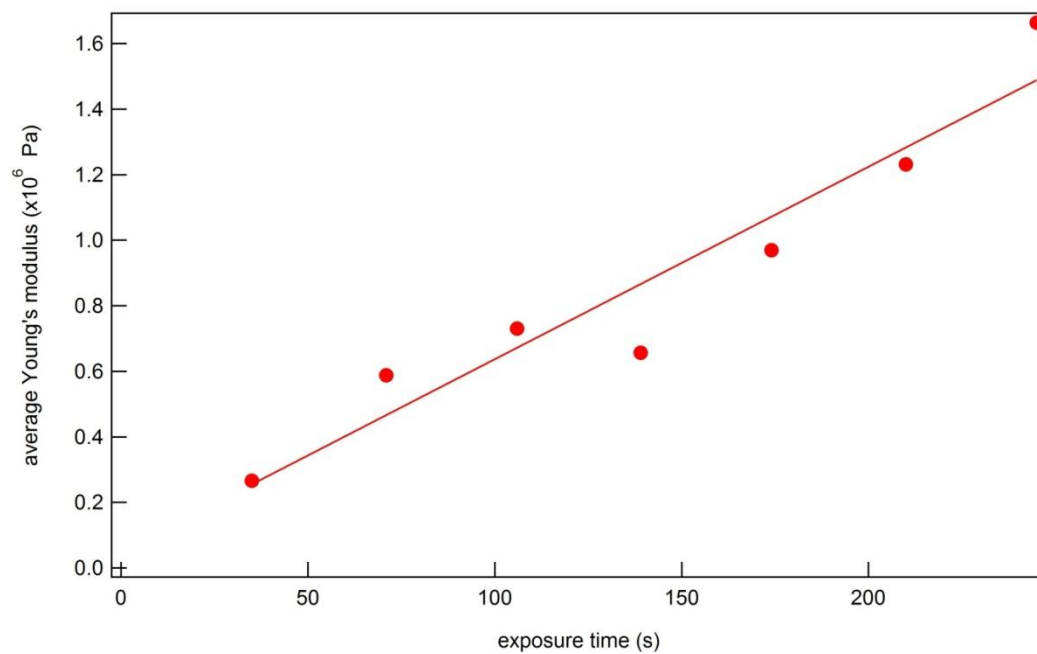
Figure: 7.2. 11: Young's modulus compared to exposure time for 1.28 μm/s.

As we expected, we see that generally as the exposure time increases, the

Young's modulus increases. For all the exposure times, increasing velocity

results in increasing Young's modulus. Generally, the Young's moduli values are

relatively constant for all velocities until approximately 2.56 μm/s. For velocities

greater than 2.56 μm/s, the Young's modulus increases with increasing velocity.

The regions exposed for 1 min 11 s (rectangle 2, see Figure 7.2.3) and for 3 min

30 s (rectangle 6, see Figure 7.2.6) do not have a plateau in the low-velocity

region as this trend would predict. Because these data are preliminary, however,

we expect that collecting more data will allow us to determine the actual average

Young's moduli and to determine better the actual trends in the data.

For the two different crosslinking regions samples, the data exhibit

considerable variability at some velocities, as evident in the standard deviation

values for the Young's modulus (see Figure 8.1.1 in section 8.1). This variability

is discussed in detail in the next chapter (sections 8.1 – 8.4).

8. DISCUSSION

OVERVIEW

In this section, I will discuss the variability in the data generally and then the effects of various experimental variables – such as evaporation of the solvent in which the AFM measurements were performed, varying ion concentration, and temperature – on the measured Young's moduli. In particular, the large standard deviations for the Young's modulus values at some velocities and the relative influence of the quantities listed above on those measured values will be discussed. I will also highlight the possible effects of viscoelasticity and poroelasticity, two time-dependent behaviors present in hydrogels. Finally, preliminary data on the relationship between UV exposure time (and, thus, crosslink density) and Young's modulus will be presented, and the general trends will be highlighted.

8.1 VARIABILITY IN THE DATA

Although the standard deviation of the Young's modulus was not negligible for any velocity, the standard deviation in the Young's modulus for the higher velocities, shown as the error bars in the plot of the average Young's modulus against the average velocity below, was nearly equal to or even larger than the mean value of the Young's modulus at that velocity. We need to

understand if actual variation in the Young's moduli, errors in the modeling, or systematic or random errors in the data acquisition is producing this measured variability in the Young's modulus.
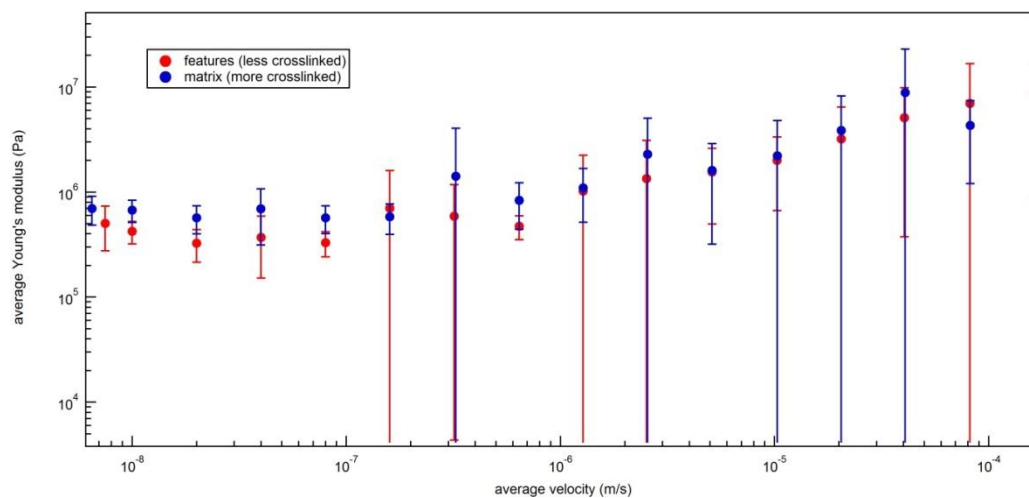
Figure 8.1. 1: Average Young's modulus plotted against average velocity withe log scales on both axes. The error bar at each point is the standard deviation.

First, the large errors bars call into question whether the two-point method outline by Ebenstein (2011) is an accurate method to extract the mechanical properties of these materials.   Although the method does account for the adhesive force, we see more variation in the Young's moduli obtained from this method than in the slope of the extension curve, which provides a qualitative sense of the mechanical properties of the material. Moreover, Ebenstein notes that the two-point method does not account for viscoelasticity, an aspect that will be discussed in more detail in section 8.5.

A related possibility is that the material may be better described at some velocities by the Maugis model rather than the JKR model.   The Tabor parameter, as described in more detail in Section 4.4.7, is used to determine

whether the JKR, Maugis, or DMT model is most appropriate. When the Tabor parameter is much larger than 5, the JKR model best describes the material. When the Tabor parameter is between 5 and 0.1, the Maugis model most accurately describes the mechanical behavior. The values of the Tabor parameter in these experiments ranged from 16 to 1416 for the less-crosslinked regions and from 8 to 582 for the more-crosslinked regions of the films. In both cases, the smaller Tabor parameter generally corresponded to the larger velocities. Although all of these values are larger than 5, some values are not very much larger than 5. Therefore, the films may not be accurately described at all velocities by the two-point method.

Third, the beam used to photo-crosslink the materials is known to be most intense at the center and may have varied over both time and space. This variation in the beam over space could result in a lower crosslink density in the regions of the film farther from the location on the film where the beam was centered. Moreover, the beam intensity can vary from sample to sample. This variation in beam intensity, however, is unlikely to have caused the three- to four-fold increase in the Young's modulus that we see in one of the samples.

Fourth, the variations in ion concentration in the fluid in which the hydrogel was immersed during measurements or even, but less probably, temperature fluctuations may have induced the gel to swell or deswell during the experiment. These two possibilities are discussed in more detail in the section 8.2 and 8.3, respectively, of this chapter.

Finally, another factor is the location in the region of the specific crosslink density being probed. Closer to the edge of a particular crosslink density, the crosslink density may no longer be homogeneous. Although we tried to take measurements approximately the thickness of the film (15 μm) from the edge of the region of particular crosslink density, the determination of the distance between measurements was an estimate made based on the width of the cantilever and the way it appeared in the optical camera. Consequently, we may have made several measurements too close to the boundary.

8.2 EVAPORATION, ION CONCENTRATION, AND DELAMINATION

Because hydrogels are polymer networks which incorporate fluid and because the fluid environment enables the novel applications of hydrogels – including controlled drug delivery devices and microassembly devices – the PNIPAm thin films were indented in neutral solutions with a pH of 7.4. Two solutions of different ion concentration were used for the different experiments. The solutions were prepared either from powder purchased from Sigma Aldrich or from a standard recipe. The powder purchased from Sigma Aldrich was mixed with deionized water so that the resulting solution was 0.318 M NaCl and 0.0027 M KCl. The second solution was prepared by dissolving 0.05 g of sodium phophate monobasic monohydrate ($NaH_2PO_4 - H_2O$), 0.17 g sodium phophate dibasic heptahydrate ($Na_2HPO_4 - 7H_2O$), and 0.058 g NaCl in 10 mL deionized water and then diluting the solution 100 times. The resulting solution was 1 mM

NaCl.

Throughout the measurements, the solvent evaporated and, in the experimental setup used in the majority of the experiments, had to be replenished several times throughout the measurements. First, the evaporation of the solvent could cause the gel to deswell, which would result in an increased modulus. Second, as the solvent evaporated, the ion concentration within the remaining fluid increased. When more solvent is added, the gel will be able to swell. But also when more solvent is added, initially the ion concentration in the fluid decreases, but the new concentration in the fluid in which the sample was immersed is still higher than that of the original solution. This increase in the ion concentration results in deswelling of the polymer network (Daly *et al.*, 2000), which would also result in an increased modulus.

For many of the thin films of hydrogels measured, the films completely delaminated – separated from the substrate – after approximately 12 hours of measurements. The delamination probably began before it was visible in the optical camera image of the film. Once the delamination was observed, measurements were confined to areas a significant distance from the visible edge of the delamination. But, if the delamination was close enough to the measurement site, an error could have been introduced into the measurement of the modulus because it would have incorporated the behavior of any air bubbles or loose film.

When tracking the experimental conditions – such as the proximity of the

time the measurement was taken to the time the sample was rehydrated – during measurements at the same velocity, the trends in the data from three samples suggest that the large standard deviations may be at least partly the result of variability in the ion concentration and the degree to which the measurement fluid had evaporated. For an average velocity of 5.11 μm/s, the standard deviation of the Young's moduli for the different samples was not large compared to the standard deviations for other velocities (see Figure 8.2.1). In the first figure, all seven points are displayed on a log scale on the y-axis in the order that they were taken. Points 1 – 4 were taken on the first sample, points 5 – 8 on the second
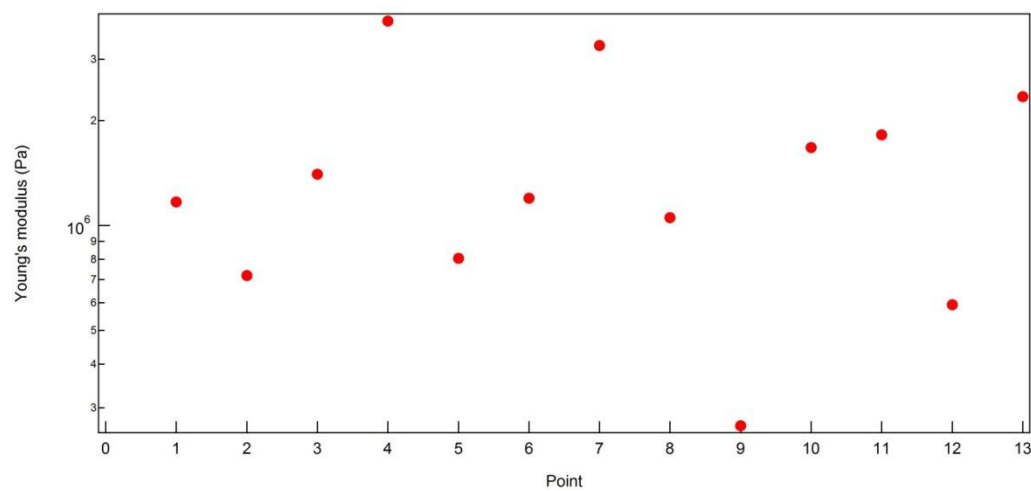
Figure 8.2. 1 Young's modulus at each point for 5.11 um/s

which points belong to which sample.
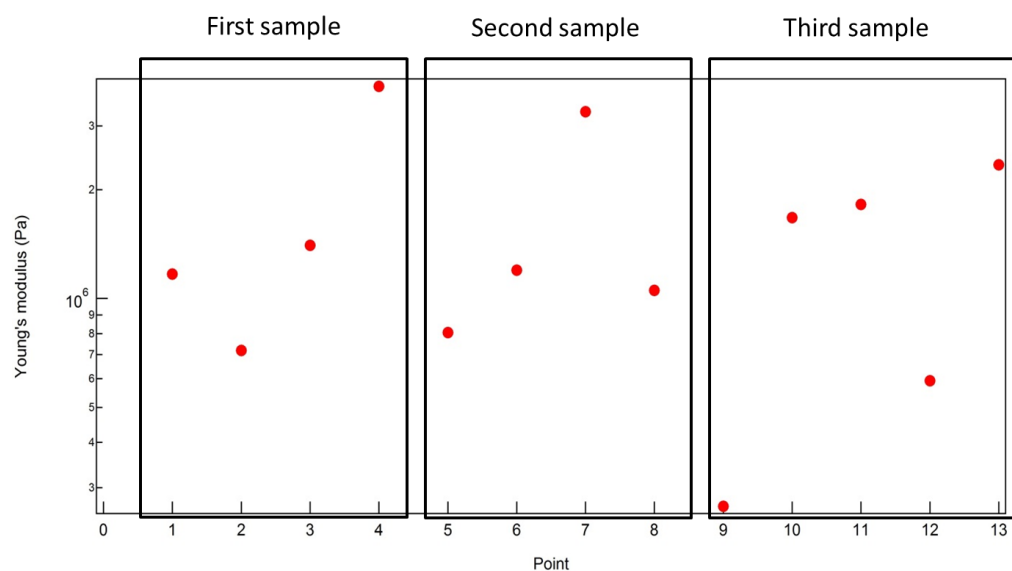
Figure 8.2. 2: Young's modulus at each point, with outlines of which point was measured on which sample.

Point	Young's modulus (Pa)
1	1.17E+06
2	7.19E+05
3	1.40E+06
4	3.86E+06
5	8.05E+05
6	1.20E+06
7	3.29E+06
8	1.05E+06
9	2.66E+05
10	1.67E+06
11	1.82E+06
12	5.93E+05
13	2.34E+06

Table 8.2 1: Table showing the Young's modulus value at each point.

The first and second plots above suggest that the outliers are points 2, 4, 7, 9, and 12. For brevity in the following discussion, the "rehydration point" is the time when the sample was rehydrated. Point 2 was taken just a little time after the

rehydration point, and we can see a decrease in modulus from point 1, which was not taken any time close to the rehydration point. Likewise, points 3, 4, and 5 were not taken any time close to a rehydration point, but point 3 was taken near the middle of the crosslink density region whereas points 4 and 5 were taken near the edge of the crosslink density region. Point 6 was taken a little after the rehydration point, but point 7 was taken with the same conditions as points 4 and 5. At point 8, the sample was starting to delaminate and to dry out. Point 9 was taken with the same conditions as points 4, 5, and 7. Points 10, 11, and 12 were taken near edge of the crosslink region. Points 10 and 11 were taken slightly before the rehydration, whereas point 12 was taken approximately the same interval of time after the rehydration point. Finally, point 13 was not measured close to the rehydration point.

These data suggest that immediately after the solvent is rehydrated, the sample's modulus decreases, a result predicted to occur with the initial decrease in ion concentration. In addition, when the sample begins to delaminate and dry out, the modulus decreases dramatically.

Likewise, data collected at an average velocity of 81.87 μm/s suggests a similar trend. Like the previous figure, in Figure 8.2.3 the Young's modulus values collected on three different samples are shown on a log scale in the order that they were taken. Points 1 – 5 were taken on the first sample, points 6 – 10 on the second sample, and points 9 – 14 on the third sample. Figure 8.2.4 highlights the points correspond to each sample.
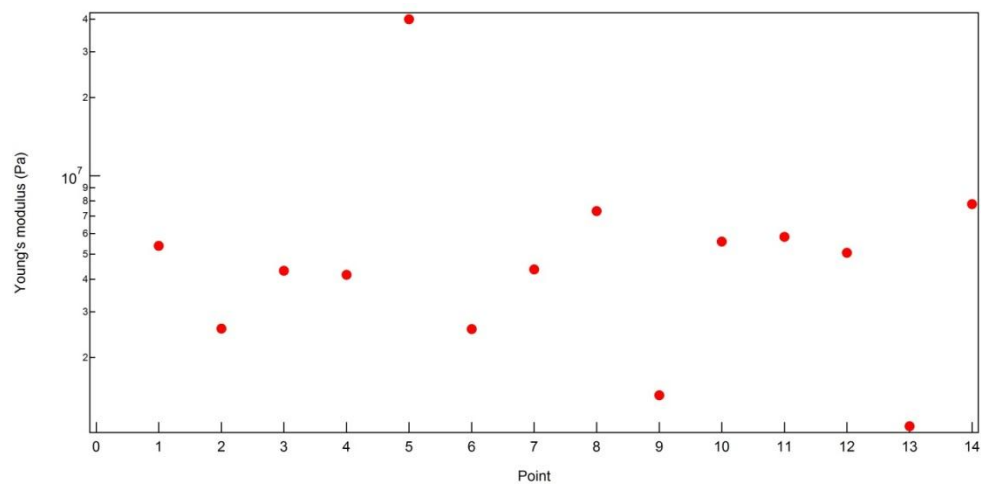
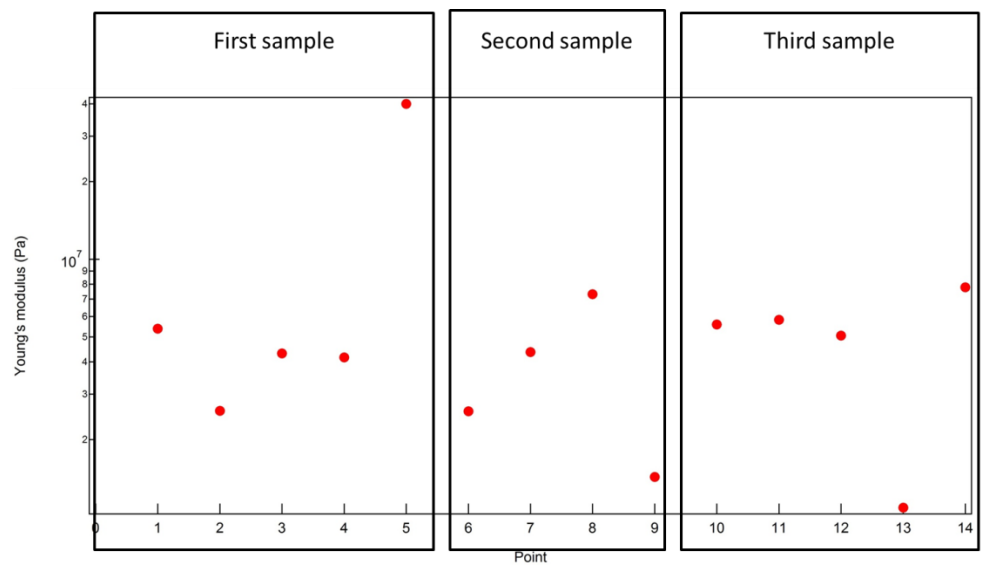Figure 8.2. 3: The Young's modulus values at each point for 81.87 um/s

Figure 8.2. 4: The Young's modulus values at each point for 81.78 um/s, where the points belonging to each sample are highlighted.

Point	Young's modulus (Pa)
1	5.38E+06
2	2.59E+06
3	4.31E+06
4	4.16E+06
5	4.00E+07

6	2.57E+06
7	4.36E+06
8	7.32E+06
9	1.43E+06
10	5.59E+06
11	5.82E+06
12	5.06E+06
13	1.09E+06
14	7.77E+06

Table 8.2 2: The Young's modulus values that correspond to each point.

Point 1 was not close to the rehydration point but was at the corner of the less crosslinked region. Point 2 was soon after the rehydration point, and we can see a corresponding decrease in the Young's modulus, as predicted by the decrease in ion concentration. Points 3, 4, 5, and 6 were not close to the rehydration point, and the modulus is correspondingly stable for points 3 and 4. Point 7 was taken within the first set of force curves after the rehydration point but was not very close to the rehydration point. Point 8 was not close to the rehydration point. When point 9 was measured, however, the sample was beginning to delaminate, and much of the solvent had evaporated. Points 10, 11, 12 and 14 were not close to the rehydration points but were measured close to the edge of the less crosslinked region. Point 13 was the second curve after rehydration.

This description in the preceding paragraph suggests that the large error bars may be due at least in part to the amount of solvent that had evaporated and the corresponding ion concentration at the time of the measurement. When all of these points are included, the standard deviation is 9.71 MPa whereas the average

Young's modulus value is 6.96 MPa. When understanding the relative contribution of each point to the standard deviation, a qualitative examination of the actual force curves is helpful. Looking at Figure 8.2.5, we can see that point 5, the sky-blue curve at the far left of the figure, has a nonlinear slope in the extension curve in contrast to the linear slopes of most extension curves. At point 9, as was stated in the previous paragraph, the sample was beginning to delaminate. The film could have actually already delaminated at the location where point 9 was located without being visible in the optical camera; thus, the tip may have had to press the film back onto the sample before being able to measure the mechanical properties of the film, rendering this point an inaccurate measure of the films mechanical properties. Moreover, the slope of the force curve at point 9, the purple curve close to the nonlinear curve of point 5, is nonlinear. Point 13 was soon after the rehydration point so that the gel did not have time to rehydrate fully. Furthermore, the blue force curve at the far right corresponding to point 13 has a much smaller slope than any of the other force curves. If we neglect points 5, 9, and 13, the average becomes 4.99 MPa, and the standard deviation is 1.65 MPa.
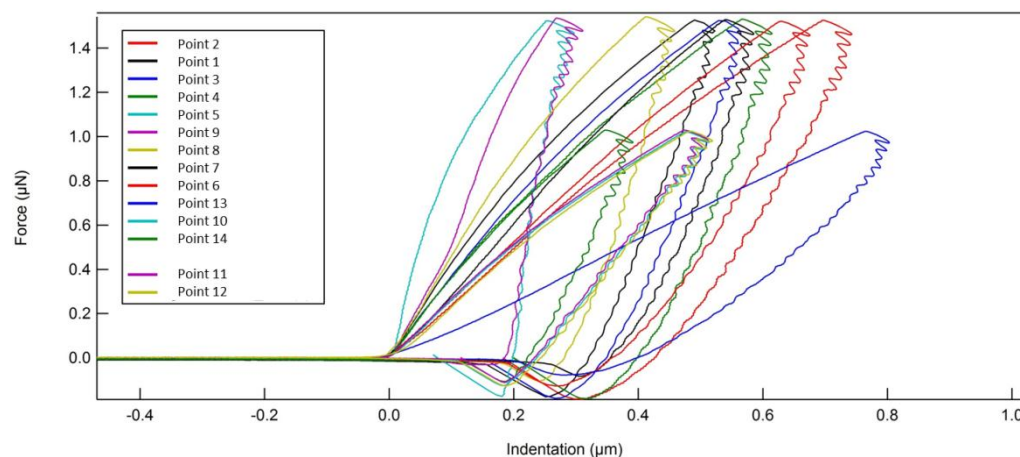
Figure 8.2. 5: Force curves for the Young's modulus values measured at 81.71 um/s.

Even by neglecting just three points, the standard deviation was decreased

dramatically, suggesting that the ion concentration and evaporation influence the

measured Young's modulus. In future experiments, it will be important to

monitor the evaporation of the solvent and to maintain a certain ion concentration.

A possible method to reduce evaporation and thereby stabilize iron concentration

is to use an enclosed fluid cell in which the temperature can be monitored.

Ongoing analysis will continue to focus on whether disregarding data points due

to their proximity to rehydration points or to the edges of the sample or to the

regions of delamination reduces variability in the measured Young's moduli.

8.3 TEMPERATURE

Much research has demonstrated that PNIPAm is responsive to

temperature (Hirotsu *et al.,* 1987). In fact, it undergoes a deswelling transition

about 37ºC (Eeckman *et al.,* 2004). Therefore, the hydrogel should become stiffer

as the temperature increases. In the first experimental setup, much less solvent

was used, and the solvent evaporated quite quickly, needing to be replenished approximately every two to three hours. This evaporation could have been hastened by heating of the solvent due to the laser deflected from the back of the tip or to the light of the optical camera used to visualize the sample.

This possibility seems less probable due to the results of the second experimental setup, in which the fluid cell was used to monitor the temperature. The temperature variation stayed within 1ºC of the initial temperature. Although this setup did allow more solvent to be used, the stability of the temperature suggests that the temperature variation in the first experimental setup was not a significant contributing factor to any variations in elastic moduli values with time.

8.4 AFM TIPS

For three out of the four measurements, the same tip was used. In between measurements, the tip was allowed to air-dry in its covered case. The tip was calibrated before measurements were taken for that day, and the spring constant measured did not vary more than 20% from 1.90 N/m, the value measured during the first set of measurements. This percentage of variation, however, is close to the uncertainty in the spring constant. Consequently, this variation is not the most important consideration. In addition, the fluctuations we observe in the Young's moduli are much larger than 20%. Thus, variations in the spring constant were not a major factor in the variability in the data. Using the same tip eliminated fluctuations in the tip spring constant as a potential variable in mechanical

properties measurements, and, since nothing unusual was observed during the calibrations, the tip was probably not a significant variable.

8.5 VISCOELASTICITY AND POROELASTICITY

These hydrogel thin films exhibit both viscoelastic and poroelastic behavior, which introduces two time-dependent characteristics into the mechanical behavior. A time-dependence was therefore expected and observed in these experiments. A log-log plot of the Young's moduli versus the rate at which force was applied is provided below:
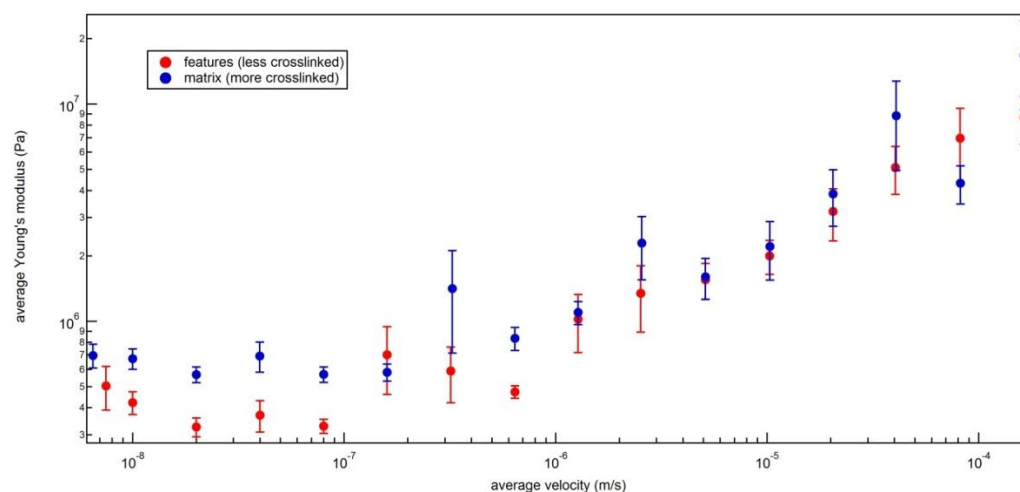
Figure 8.5. 1: Average Young's modulus plotted against the average velocity, where both axes use log scales.

This plot reveals that the Young's modulus appears to be stable in the low-velocity regime for both the less-crosslinked and more-crosslinked regions on the different samples. The Young's modulus increases with velocity. In fact, in these plots, the Young's modulus of the material increases slightly more than an order of magnitude. The question that arises is what causes this apparent stiffening of

the material at high rates of force application.

Viscoelasticity is a property of the majority of polymers. A viscoelastic material acts as an elastic solid when stress is applied quickly. When stress is applied slowly, the chains in a polymer solution will flow viscously to relieve the stress. In a polymer hydrogel, the polymer chains are held in place by the crosslinks, but, when stress is applied slowly, the chains have time to relax as force is applied. The simplest model of the mechanical behavior of a viscoelastic material, also called the Maxwell model, is a spring in series with a dashpot (Lin, 51-61), a mechanical buffer consisting of piston operating within a cylinder of viscous fluid (*Oxford English Dictionary*, dash, v.1). The spring represents the elastic behavior of the material because it stores mechanical energy as the system is stressed. In contrast, the dashpot represents the viscous behavior of the material since it dissipates energy when the system undergoes stress. The relaxation time of a viscoelastic system modeled in this way is the ratio of the viscosity of the material and the modulus of the material (Lin, 51-61).

For a purely viscoelastic material, the modulus can change by orders of magnitude as the rate at which stress is applied is varied. As the rate at which the force is applied increases, the polymer chains do not have time to relax. Thus, the force resisting deformation increases, and the material appears to stiffen.

Recently, poroelasticity has been identified as a significant behavior of hydrogels (Galli *et al.,* 2009). Poroelasticity is the movement of the solvent induced by the deformation of the hydrogel network (Cai *et al.,* 2010). The

mechanical behavior of poroelastic materials, including hydrogels, is adequately described by Biot's theory of linear poroelasticity. Previously, Yoon and coworkers have demonstrated that Biot's theory predicts accurately the swelling behavior of both free-floating PNIPAm hydrogels and hydrogels attached to a substrate. They found that perturbations travel a distance given by the square root of the diffusivity D and the time t during which the movement of the perturbation is observed (Yoon *et al.,* 2010).

This mechanism introduces additional time dependence to the mechanical behavior and a decrease in the Young's modulus with time. If the network is pressed quickly enough, the solvent will not have time to migrate away from the tip. With time, however, solvent is able to migrate, and the material will appear to soften. This decrease in modulus, however, is expected to be approximately 15%, rather less than the order of magnitude that was observed in these samples.

The mechanical behavior for both the more-crosslinked regions and the less-crosslinked regions of the films, therefore, seems to be a combination of poroelasticity and viscoelasticity. In the low velocity regime, the solvent has time to migrate fully away from the tip, and the relaxation of the polymer chains within the network can be probed. As the velocity increases, the solvent, essentially water, will diffuse rapidly but eventually will not have enough time to diffuse completely, resulting in an apparent stiffening of the sample. Likewise, the polymer chains do not have enough time to relax fully, resulting in a stiffening of the sample. Although initially negligible, viscoelasticity and poroelasticity will

contribute to the apparent stiffening of the materials at higher velocities.

The experimental results suggest that this explanation is plausible. These data show that the Young's modulus is relatively constant at low velocities, regardless of the crosslink density in that region. In this region, viscoelastic and poroelastic effects are negligible. For higher velocities, the data is not sufficient to determine the velocity at which poroelastic effects or viscoelastic effects become significant. Nor can the data determine conclusively if the possible explanation given in the preceding paragraph is an accurate description. In the future, this description could be tested by indenting the film to different depths and recording the relaxation time. If the material is poroelastic, the relaxation time should vary with the square of the indent depth (Yoon *et al.,* 2010). But if the material is viscoelastic, the relaxation time is independent of the indent depth (Lin, 54). In addition, these data are not conclusive about whether there is also a plateau in the Young's modulus values at very high velocities, as would be expected for viscoelastic materials (Lin, 60-61). Higher velocities, in fact, were not probed due to limits on the speed from the AFM.

As noted in section 8.1, the two-point method, a relatively simple method to apply the JKR model to force curves and extract mechanical properties, does not account for the effects of viscoelasticity on the measured moduli. In fact, this method will be inaccurate if the time needed for the polymers to relax is longer than the total possible indentation time. Moreover, this method does not account for poroelasticity (Ebenstein, 2011). As discussed in the previous paragraphs of

this section, however, the viscoelastic and poroelastic effects are negligible in the low-velocity regime. Thus, the two-point method can provide accurate measurements of the Young's moduli in this regime. At the higher velocities, we do not know the exact regime where the viscoelastic effects, poroelastic effects, or both become significant. More research should be done to study viscoelasticity and poroelasticity in hydrogels. Regardless, both effects are negligible in the low-velocity regime, and, thus, the two-point method and its results are still valid in that regime.

While the mechanical properties of the polymer network is probably most evident at the low velocities, measurements of the time-dependent physical responses of these materials are important. First, these materials will be incorporated in a variety of applications, such as controlled drug delivery devices or sensors or actuators in microfluidic systems. In these applications, the rate at which force is applied will not always be within the low-velocity regime, and an understanding of the apparent stiffness of the material at those rates will be important. Second, this apparent stiffening of the material at swift rates of application of force could be utilized. For instance, in a microassembly device, the hydrogels' apparent stiffening could be used to slow down the rate at which materials that would otherwise collapse in on each other were assembled.

8.6 RELATIONSHIP BETWEEN CROSSLINK DENSITY AND YOUNG'S MODULUS

Preliminary data from the single hydrogel film containing seven rectangles of varying exposure time, resulting in seven different crosslink densities, suggests that the Young's modulus increases with increasing crosslink density, as is evident in the following two figures. The first figure shows the average modulus values taken at 80 nm/s, and the second similarly shows the average modulus values taken at 1.28 μm/s. The exact relationship cannot be determined from these preliminary results, but future research should be able to determine the relationship more precisely.
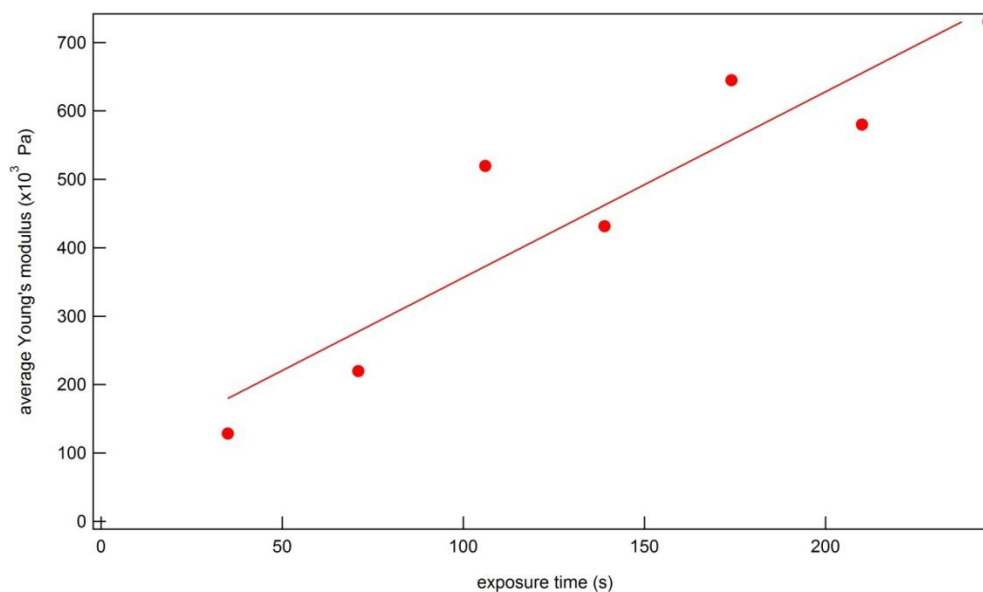

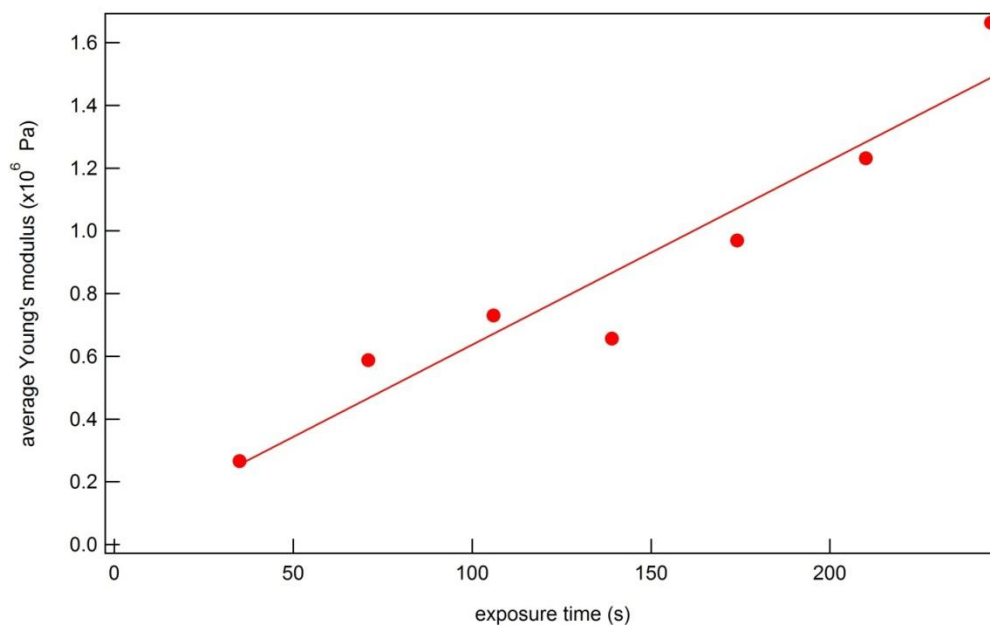Figure 8.5. 2: Trend in Young's modulus with exposure time for 80 nm/s.

Figure 8.5. 3: Trend in Young's modulus with exposure time for 1.28 um/s.

9. CONCLUSIONS AND FUTURE DIRECTIONS

In this research, we measured the Young's modulus of thin films of photo-crosslinkable PNIPAm using AFM. We found that the Young's modulus is relatively constant in the low-velocity regime but increases dramatically as the velocity increases. In the range of velocities that was probed, we saw more than an order of magnitude change in the Young's modulus value. At low velocities, the Young's modulus has negligible time dependence as expected since the material has the time to relax fully; therefore, viscoelastic and poroelastic effects are negligible in that regime. Consequently, the measurements of the modulus are measurements of the elasticity of the polymer network. This elasticity results from the changes in entropy of the polymer chains in the network occurring when the network is deformed (Lin, 17-18).

We do not have enough data, however, to determine whether poroelasticity, viscoelasticity, or a combination of the two is responsible for the increase in the elastic modulus with increasing velocity. Moreover, we cannot determine if the elastic modulus will again be constant at high velocities, as is expected for both a purely viscoelastic material (Lin, 58-61) and a purely poroelastic material (Yoon *et al.*, 2010).

The variability in the data could be the result of several possible causes. First, we may be closer to the transition zone between JKR and Maugis models

that we realized. Second, the two point method may not be an accurate description of these materials. Third, the ultraviolet light intensity used to photo-crosslink the materials may have varied over both time and space, resulting in a less even crosslink density than we realized. Fourth, the variations in ion concentration in the fluid in which the hydrogel was immersed during measurements or even, but less probably, temperature fluctuations may have induced the gel to swell or deswell during the experiment rather than the gel remaining in equilibrium throughout the experiment.

We also measured thin films with 7 different crosslink densities. We again saw a very similar trend in the Young's modulus as the films with only 2 crosslink densities. In addition, we observed a gradual increase in the elastic modulus across all velocities as the crosslink density increases. This data is still preliminary and should be corroborated by additional measurements.

Possible future directions for this project can be divided into two main categories. First, we need to understand the variability in the data. We need to improve our measurement technique and reevaluate the sample preparation procedure. The biggest variable that was not controlled in these experiments was ion concentration. Therefore, at the very least, the ion concentration should be better controlled in the future. To control evaporation and monitor temperature, a semi-enclosed stage could be used. Also, we will continue to take data so that the average value can be better established. Moreover, the current model needs to be evaluated and improved to describe our data more accurately. One possible

method could be a full or partial curve fit. Furthermore, the Maugis model could be applied to the force curves to see if that model produces a more accurate result.

Second, many more physical relationships should be probed. One possibility is to investigate the exact relationship between the ion concentration and the Young's modulus. The relationship between temperature and Young's modulus should also be probed. The JKR model does not address viscoelasticity or poroelasticity. Consequently, the viscoelastic and poroelastic behavior should be probed, possibly using varying indentation depths and measurement times to do so.

10. REFERENCES

Bashir, R., Hilt, J.Z., Elibol, O., Gupta, A., and Peppas, N.A. Micromechanical cantilever as an ultrasensitive pH microsensor. **81**, *Applied Physics Letters,* 3091-3093, 2002.

Beebe, D.J., Moore, J.S., Yu, Q., Liu, R.H., Kraft, M.L., Jo, B., and Devadoss, C. Microfluidic tectonics: A comprehensive construction platform for microfluidic systems. **97**, *Proc. Natl. Acad. Sci.* (USA), 1348, 2000.

Cai, S., Hu, Y., Zhao, X., and Suo, Z. Poroelasticity of a covalently crosslinked alginate hydrogel under compression. **108,** *J. Appl. Phys.,* 113514, 2010.

Carracher, Charles E., Jr. *Introduction to Polymer Chemistry.* 2nd ed. Boca Raton, FL: CRC Press, 2010.

Carrillo, F., Gupta, S., Balooch, M., Marshall, S.J., Marshall, G.W., Pruitt, L., and Puttlitz, C.M. Nanoindentation of polydimethylsiloxane elastomers: Effect of crosslinking, work of adhesion and fluid environment on elastic modulus. **20,** *J. Mater. Res.,* 2820-2830, 2005.

Cao, Y., Yang, D. and Soboyejoy, W. Nanoindentation method for determining the intial contact and adhesion characterisitcs of soft polydimethylsiloxane. **20,** *J. Mater. Res.,* 2004-2011, 2005.

Cowie, J.M.G. and Valeria Arrighi. *Polymers: Chemistry and Physics of Modern Materials.* Boca Raton, FL: CRC Press, 2008.

Dashpot. (2012). *Oxford English Dictionary* (2nd ed.). Retrieved 15 April 2012, from http://www.oed.com/view/Entry/47368

Duncan, R. **2,** *Nat. Rev. Drug Discovery,* 347, 2003.

Ebenstein, D.M. Nano-JKR force curve method overcomes challenges of surface detection and adhesion for nanoindentation of a compliant polymer in air and water. **26,** *J. Mater. Res.,* 1026-1035, 2011.

Eaton, Peter and Paul West. *Atomic Force Microscopy.* Oxford: Oxford University Press, 2010.

Eeckman, F., Moes, A., and Amighi, K. Synthesis and characterization of

thermosensitive copolymers for oral controlled drug delivery. **40,** *European Polymer Journal,* 873, 2004.

Galli, K. Comley, T.A.V. Shean, and M.L. Oyen. Viscoelastic and poroelastic mechanical characterization of hydrated gels. *J.Mater.Res.,* **24,** 973, 2009.

Gilbert, Thomas R., Rein V. Kirss, Natalie Foster, and Geoffrey Davies. *Chemistry: the Science in Context.* 2nd ed. New York: W.W. Norton & Company, Inc., 2009.

Hibbler, R.C. *Mechanics of Materials,* 5th ed. Upper Saddle River, NJ: Pearson Education, Inc., 2003.

Hilt, J.Z., Gupta, A.K., Bashir, R., and Peppas, N.A. Ultrasensitive Biomems Sensors Based on Microcantilevers Patterned with Environmentally Responsive Hydrogels. **5,** *Biomedical Microdevices,* 177-184, 2003.

Hirotsu, S., Hirokawa, Y., and Tanaka, T. **87,** *J. Chem. Phys.,* 1392, 1987.

Hu, Y., Chan, E.P., Vlassak, J.J., and Suo, Z. Poroelastic relaxation indentation of thin layers in gels. **110,** *J. App. Phys.,* 086103-1 – 086103-3, 2011.

Johnson, K.L. *Contact Mechanics.* Cambridge, UK: Cambridge University Press, 1985.

Johnson, K.L., Kendall, K., and Roberts, A.D. Surface energy and the contact of elastic solids. **324**, *Proc. R. Soc. Lond.* A., 301-313, 1971.

Kranenburg, J.M., Tweedie, C.A., van Vliet, K.J., and Schubert, U.S. Challenges and Progress in High-Throughput Screening of Polymer Mechanical Properties by Indentation. **21,** *Adv. Mater.,* 3551-3561, 2009.

Kim, J., Yoon, J., and Hayward, R.C. Dynamic display of biomolecular patters through an elastic creasing instability of stimuli-responsive hydrogels. **9,** *Nature Materials,* 159-164, 2010.

Lin, Yn-Hwang. *Polymer Viscoelasticity.* 2nd ed. Hackensack, NJ: World Scientific Publishing Co. Pte. Ltd., 2011.

Maugis, D. Adhesion of Spheres: The JKR-DMT Transition Using a Dugdale Model. **150,** *Journal of Colloid and Interface Science*, 243-269, 1992.

Shibayama, M. and Tanaka, T. *Volume Phase Transition and Related Phenomena of Polymer Gels.* **109,** *Advances in Polymer Science,*1-62,

1993.

Tabor, D. Surface Forces and Surface Interactions. **58,** *Journal of Colloid and Interface Science,* 2-13, 1977.

Tanaka, T. Chapter 1. *Phase Transitions in Gels* in *Polyelectrolyte Gels: Properties, Preparation, and Applications. Ed.* Ronald S. Harland and Robert K. Prud'homme. **December 4, 1992**, 1-21.

Toomey, R., Freidank, D., and Rühe, J. Swelling Behavior of Thin, Surface-Attached Polymer Networks. **37,** *Macromolecules,* 882-887, 2004.

Yoon, J., Cai, S., Suo, Z., and Hayward, R.C. Poroelastic swelling kinetics of thin hydrogel layers: comparison of theory and experiment. **6,** *Soft Matter*, 6004-6012, 2010.

Zhang, Y., Ji, H., Snow, D., Sterling, R., and Brown, G.M. A pH Sensor Based on a Microcantilever Coated with Intelligent Hydrogel. **32,** *Intrumentation Science and Technology,* 361-369, 2004.